The development of a cost-effective beam loss monitor for use at the K600 magnetic spectrometer at iThemba LABS

Stanley Douglas Walton

A thesis submitted to the Faculty of Science at the University of Cape Town in fulfillment of the requirements for the degree of Master of Science

February 2008

Abstract

The purpose of this work was to develop a cost-effective beam loss monitor for use at the K600 magnetic spectrometer at iThemba LABS. To this end, the commonly used materials and technologies were reviewed, and photodiodes were chosen because of their low price, high performance and ready availability. Experiments have been carried out and compared to theoretical calculations. Recommendations for future developments are presented.

Declaration

1. I know that plagiarism is wrong. Plagiarism is to use another's work and to pretend that it is one's own.
2. I have used an accepted convention for citation and referencing. In this thesis, each significant contribution or quotation from the work or works of other people has been attributed, and cited or referenced.
3. This thesis is my own work.
4. I have not allowed, and will not allow, anyone to copy my work with the intention of passing it off as his or her own work.

Stanley Walton

Acknowledgements

I would like to acknowledge the people who helped me along the way...

- My supervisor, Professor Fearick, for his guidance over the years.
- From iThemba LABS: Ricky Smit, Retief Neveling and Ziggy Fortsch, for their tireless assistance with experimental matters.
- R.A.J. Parry and V. Monadjem, for their expertise in electronics.
- Andrea Prinsloo and Maciek Stankiewicz, for their insightful criticism.
- Bonnie, for her love and support.
- Most of all, my parents, for their unwavering support for that past 26 years.

Contents

Chapter 1

Introduction

1.1 iThemba LABS cyclotron facility

South Africa's iThemba LABS (formerly the National Accelerator Centre), located 30 km outside Cape Town, is the premier particle accelerator facility in Africa. The activities undertaken at iThemba LABS include commercial radioisotope production, radiation therapy for cancer patients and fundamental nuclear physics research.

Accelerated protons and other light ions are delivered by the main accelerator, which is a separated sector cyclotron (SSC). The SSC has a K factor of 200, which means it can accelerate protons to an energy of 200 MeV.

The SSC works 24 hours a day, seven days a week, except for a few weeks of planned downtime per year, as well as for occasional periods of unplanned downtime due to power outages. Weekdays are devoted to therapy – proton and neutron, whereas weeknights are for radioisotope production. Beam time from 16h00 on a Friday until 08h00 on the following Monday is dedicated to nuclear physics experiments [20]. During these times, the beam is delivered to one of several instrumentation vaults, including the AFRODITE vault for γ spectroscopy and the K600 magnetic spectrometer vault. Figure 1.1 shows the layout of the iThemba LABS cyclotron facility.

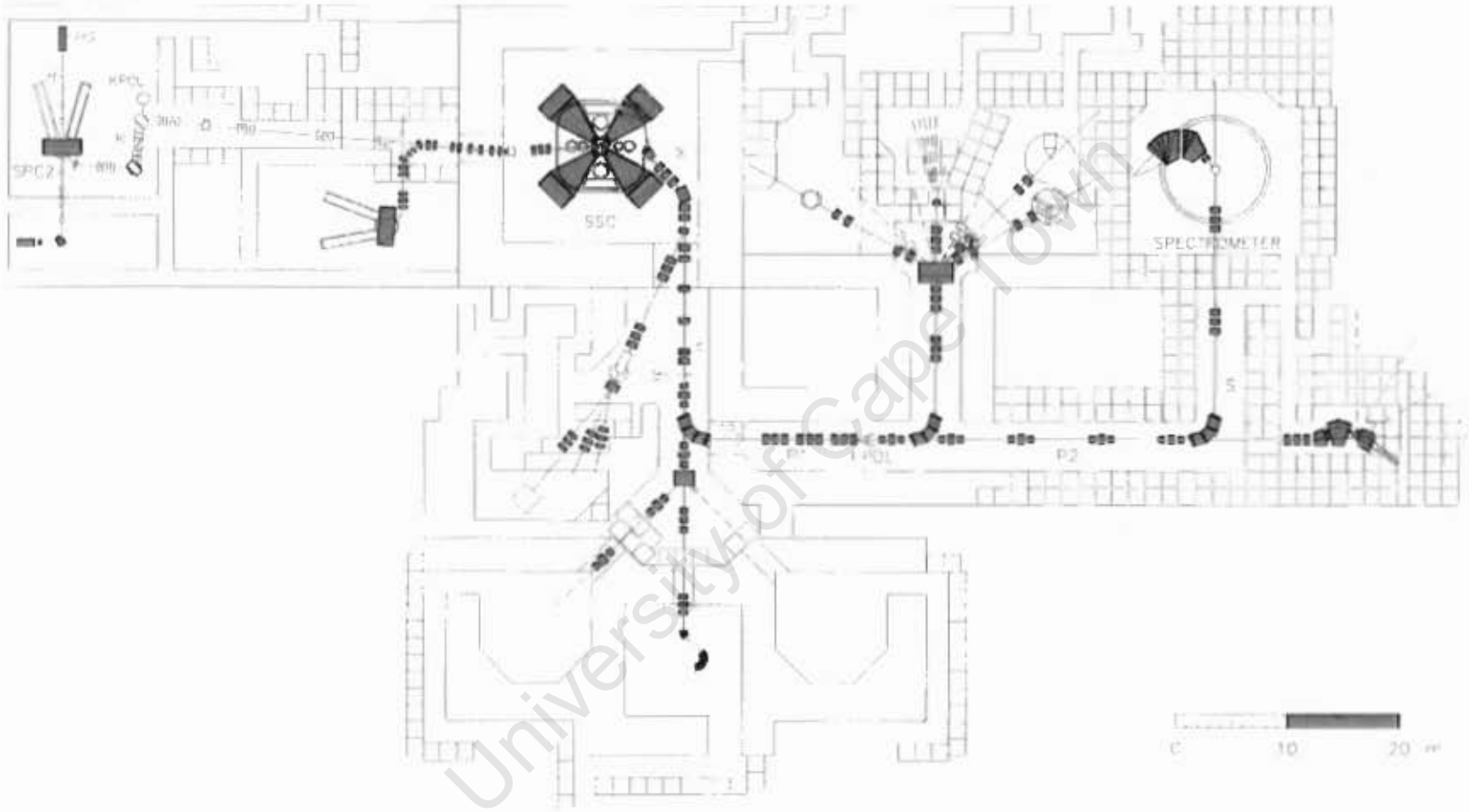

Figure 1.1: Schematic diagram of the cyclotron facility at iThemba LABS. Available at `http://k600.tlabs.ac.za`.

1.2 K600 magnetic spectrometer

Having been pre-accelerated in a K=8 solid-pole injector cyclotron, protons enter the SSC, where they orbit in the RF and magnetic fields, gaining energy with each revolution. Once they reach the extraction radius, they are directed to the spectrometer vault, using bending magnets.

Figure 1.2 shows a schematic diagram of the K600 magnetic spectrometer. Its design follows from that of the K600 at the Indiana University Cyclotron Facility (IUCF). The ion-optical system of the K600 consists of five active elements. These are a quadrupole magnet, two horizontally-bending dipole magnets and two correction coils, known as the K- and H- coils.

Protons (or other light ions), delivered to the spectrometer vault from the SSC, enter a 524 mm diameter scattering chamber, which is located on the turning axis of the K600. After interacting with the target material in the scattering chamber, some of the protons are scattered into the spectrometer. The horizontally-bending magnets, Dipole 1 and Dipole 2, bend the path of the beam into a circle of radius 2.1 m. The K-coil is a quadrupole element used for making first order kinematic corrections, while the H-coil is a hexapole element used to correct for higher order variations in momentum [14, 21].

The centre of the focal plane of the spectrometer is located 1.5 m downstream from the end of Dipole 2. The focal plane detector package is used for particle identification and momentum measurement. At the time of writing, the detector package consisted of two multi-wire drift chambers and two plastic scintillator paddles. While a brief description of the drift chambers will be given here, the paddles will not be discussed, as the operating principles of scintillators will be treated in detail in Chapter 2.

A drift chamber is a multi-wire proportional counter [11]. It consists of a row of anode wires between two cathode planes, and contains a gas which is ionised by light ions from the spectrometer. Electrons, having been liberated from atoms of the gas due to interaction with passing ions, and finding themselves in the electric field of the drift chamber, drift towards the nearest wires. Since the protons are much faster than the drifting electrons, the paddles can be used as triggers, despite their being downstream from the drift chambers. For example, a 60 MeV proton can travel from the drift chambers to the paddles in approximately 50 ns, whereas the electrons have drift times

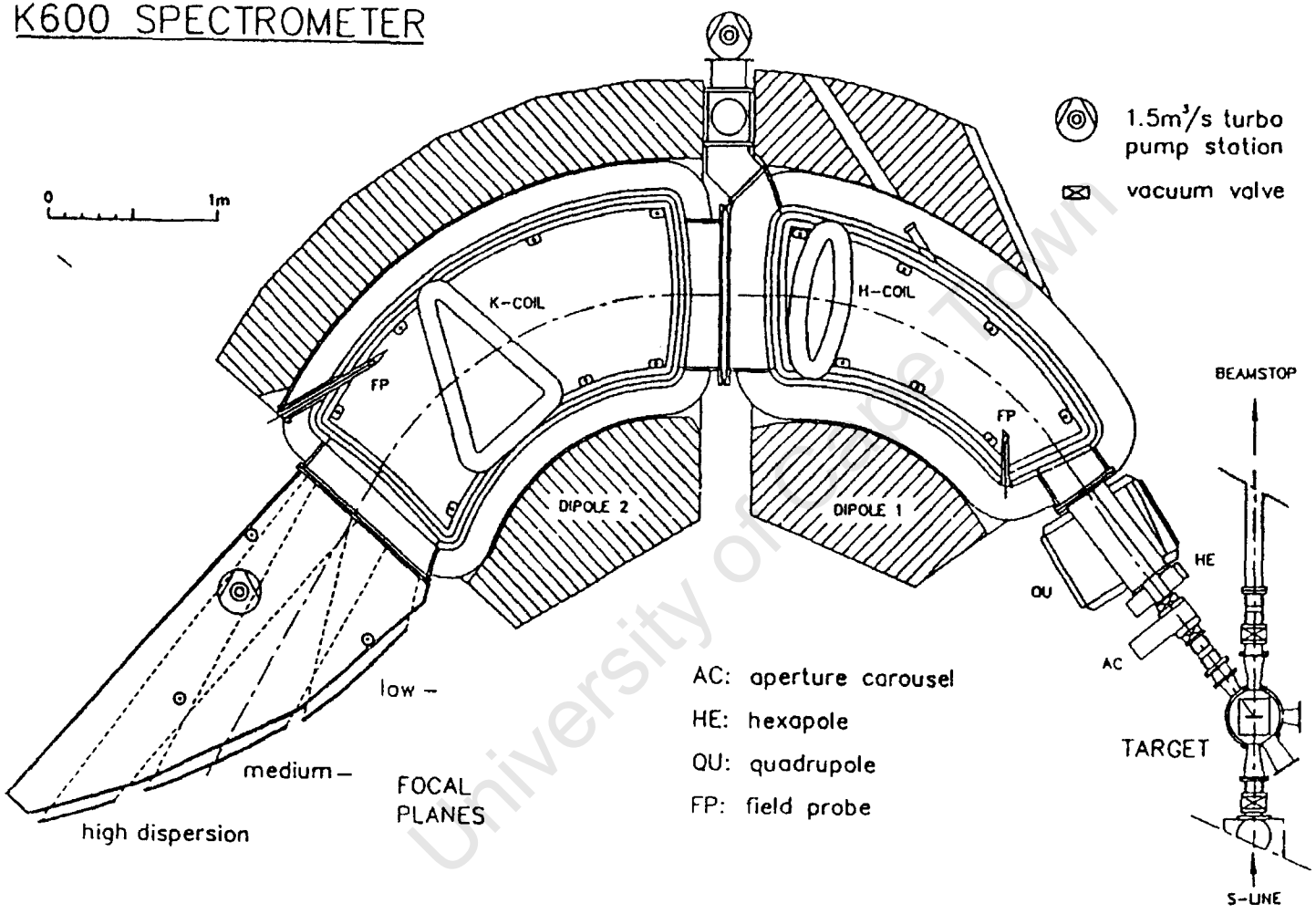

Figure 1.2: Schematic diagram of the K600 magnetic spectrometer [21].

on the order of μs. As electrons reach a wire, current flows through it and a signal is measured. Using the time taken by the electrons to reach their destination wires, as measured from the instant the paddles fire, it is possible to reconstruct the path of the ionising particle, and so to determine its energy and momentum, which yields information about the structure of the target material. Figure 1.3 shows the schematic layout of a typical drift chamber.

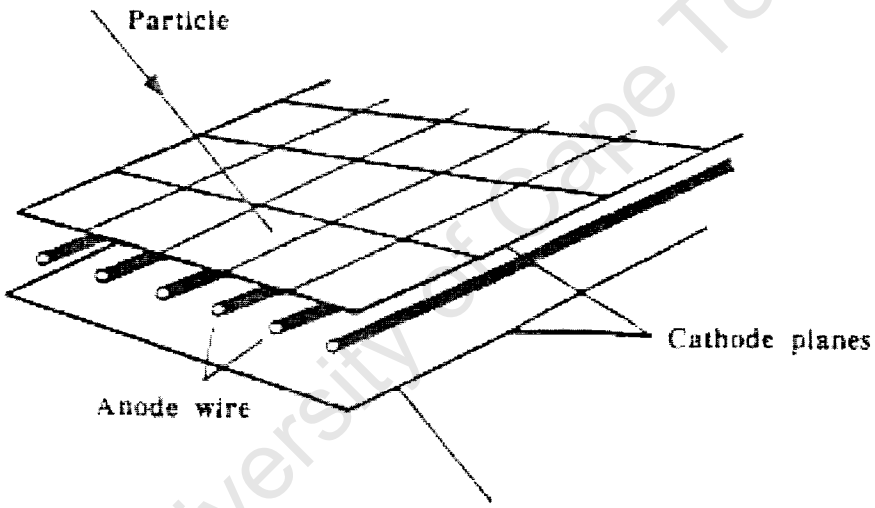

Figure 1.3: Schematic layout of a drift chamber. This work is in the public domain. See `http://en.wikipedia.org/wiki/Image:Wire_chamber.gif`.

The wires in the K600 detector package drift chambers are 20 μm gauge, gold-plated tungsten. The cathode planes are aluminised biaxially-orientated polyethylene terephthalate, also known as boPET. boPET, often called by one of its popular trade names, Mylar, has many properties which make it suitable for this application, including high tensile strength and transparency, as well as being a good gas barrier. Since it is also a good electrical insulator, metallisation, and in this case, aluminisation is necessary to ensure good electrical conductivity. The gas in these drift chambers is a mixture of 90% Ar and 10% CO_2.

1.3 Background problems in the K600

Background is a term used to describe unwanted or unimportant components of a data set. In the K600, there are many possible sources of background. It may result from effects in the electronics, such as poor grounding, a dirty or unstable power supply, or perhaps pickup of transient electric fields. Figure 1.4 shows some experimental data taken on the K600 on 2007-10-04. This experiment involved a 68.5 MeV proton beam

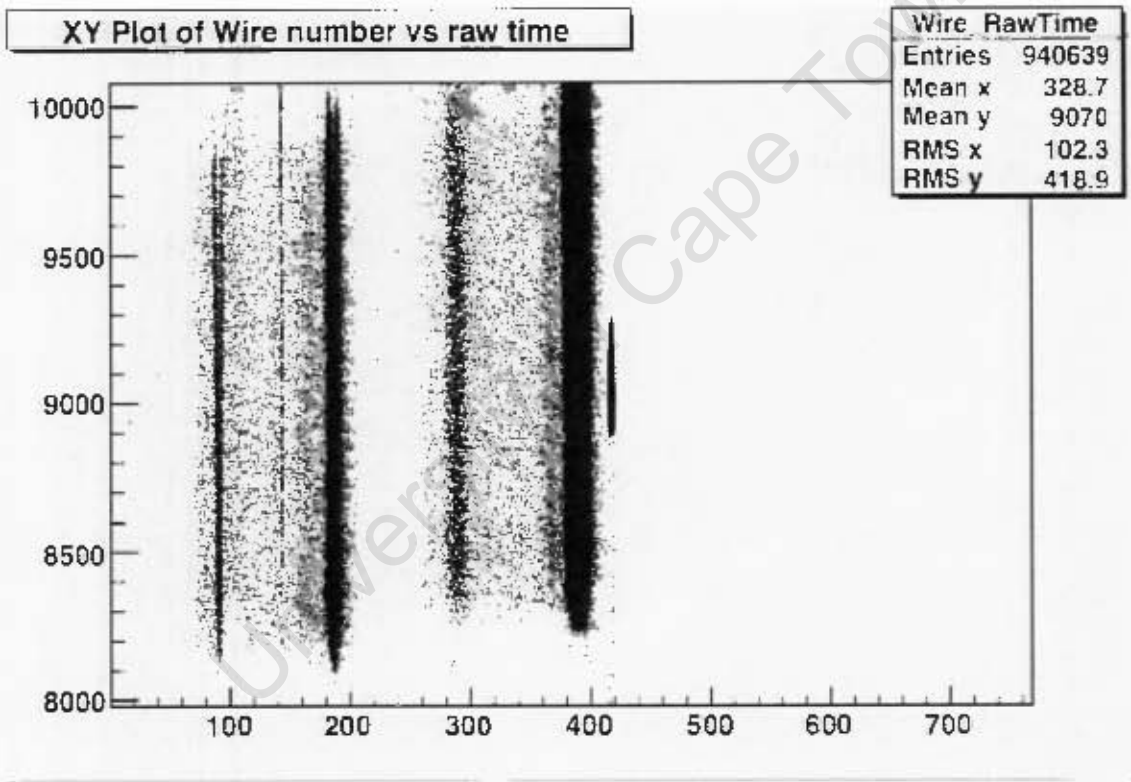

Figure 1.4: Background in K600 experimental data. The focal plane analyser module sorts through experimental data and generates the plot using ROOT [7].

incident on a ^{12}C target of thickness 40-45 mg/cm^2. The dark lines represent physically meaningful data, while the scattered dots between the dark lines are meaningless background.

Another source of background is beam halo, which refers to the cloud of particles in the outer part of the beam. Halo causes significant background problems, since the particles tend to collide with unintended targets, such as the walls of the beam pipe or

the target chamber. Each time such an unexpected collision occurs, other particles may be scattered into the spectrometer and cause the detection of "false" events by the focal plane detector package. A significant consequence of background is an increase in the uncertainty associated with measurements. A possible solution to this problem could be to deploy beam loss monitors, which will be introduced in Chapter 2.

1.3.1 Background at zero degrees

The K600 can be rotated about its axis in order to study nuclear reactions from different scattering angles. Modifications are currently underway to allow operation at an angle of 0°. These modifications include the installation of a new beam dump, as well as the development of new focal plane detectors [17], which will provide the improved vertical resolution required for zero degree measurements [18].

The quest for zero degree mode has given rise to a renewed sense of the importance of background reduction. Unlike finite scattering angle experiments, when taking measurements at zero degrees, the majority of the beam enters the spectrometer. In such a situation, the number of events is expected to be greatly increased, hence the need to reduce the amount of spurious data. It is thought that beam loss monitors will be useful in reducing background levels at zero degrees by aiding in beam focusing.

1.4 Thesis objectives and structure

The objective of this thesis is to describe the development of a cost-effective beam loss monitor, which is intended to be used at the K600 magnetic spectrometer at iThemba LABS. The beam loss monitor will be used to improve the beam characteristics by allowing the users to carefully monitor the beam profile. It is thought that this may result in lower background readings and a general improvement in the quality of experimental data.

The structure of the remaining chapters is as follows: Chapter 2 comprises a review of some of the material and technologies commonly used in radiation detection. Scintillators are treated first, followed by photomultiplier tubes and photodiodes. The design

of a simple charge-sensitive preamplifier is introduced. Chapter 3 contains a description of the beam loss monitor designs, as well as the experiments which were carried out to test them at iThemba LABS. Methods of signal processing are derived from an RC circuit analysis, and the experimental results are compared with theoretical expectations. Chapter 4 is used to present recommendations for future development, while Chapter 5 contains a few concluding remarks.

Chapter 2

Beam loss monitors: detector materials and technologies

Due to the background problems experienced by researchers at iThemba LABS, there has been much interest in the development of a cost-effective beam loss monitor, also known as a background monitor or halo monitor. A beam loss monitor is a radiation detector, which would usually be placed upstream of the target, near the beam line. When the monitor experiences a high count rate, this is an indication that the beam requires tuning.

Beam loss monitors are commercially available, but at such a high unit cost that placing monitors along the beam line in sufficient numbers would be prohibitively expensive. The development of a low-cost monitor would permit a rather liberal deployment of monitors along the beam line, which would surely aid in the delivery of high quality beam.

Beam loss monitors could be based on any radiation detection technology; the choice of which to use was primarily determined by the specific requirements of the application. The present chapter shall constitute a review of the the materials and technologies which were considered. The excellent texts by Knoll [10] and Leo [11] were used in reviewing scintillation materials, photomultiplier tubes and semiconductors.

2.1 Scintillators

Scintillation materials are those which emit visible light by prompt fluorescence when excited by ionising radiation. In order for a scintillator to be useful for radiation detection, it must satisfy several requirements.

The material must have a high scintillation efficiency. That is, it should convert as much of the deposited energy as possible to visible light. High efficiency is required to aid in the conversion of scintillation light to electrical signals. The dependence of the light output on the deposited energy should be linear, or as close to linear as possible over a maximum range of energies. The material should be transparent to its own scintillation light, for otherwise the light would be reabsorbed before reaching the light detector.

The light emission should decay sufficiently quickly as to allow fast signals to be measured. This property distinguishes prompt fluorescence from other forms of luminescence. For example, phosphorescence is the emission of longer wavelength light than is characteristic of prompt fluorescence, and with longer decay times. Delayed fluorescence is similar to prompt fluorescence, except that it also results in long decay times. Typically, scintillating materials exhibit each of these forms of luminescence, to varying degrees. To be useful in radiation detection, the scintillator should convert as little of the deposited energy as possible to light through phosphorescence and delayed fluorescence, while maximising the fraction of energy going to prompt fluorescence.

2.1.1 Inorganic scintillators

Inorganic crystals with activators

The most common form of inorganic scintillator is the activated, or doped crystal. This consists of an inorganic crystal, usually an alkali halide, to which impurities have been added. The classic example of an activated inorganic crystal is thallium-activated sodium iodide, NaI(Tl), which has been the prevailing option since its discovery, and which has the highest light yield of any known scintillator.

In crystals, electrons are restricted to a discrete set of energy bands. The lowest energy band, which contains bound electrons, is known as the valence band. The con-

duction band contains more energetic electrons, which can move around the crystal. It should be noted that in insulators, the conduction band is generally empty, apart from a few thermally excited electrons. The band gap between the valence and conduction bands is known as the forbidden band — so called because electrons in pure crystals can never be found there. It is possible for conduction electrons to be de-excited via photon emission, thereby reverting to valence electrons. However, this process is inefficient in pure crystals. In addition to the inefficiency of de-excitation, it should also be noted that band gaps in pure crystals are typically so large that the frequencies of any photons emitted as a result of this process would be in the ultraviolet range or above. Clearly, visible photons are required for scintillation. Consequently, pure crystals are not useful in scintillation applications.

It was discovered by Woodyard in the 1940s that by introducing small amounts of impurities into a semiconductor, one could modify its electrical properties [23]. This process, which later became known as doping, has made it possible to use inorganic crystals as scintillators. The presence of the doping material has the effect of altering the energy band structure, resulting in the creation of accessible energy states in the forbidden band. The band structure is shown in Figure 2.1. Since the gap between excited states and the ground state is smaller in the modified band structure, the photons which are emitted by doped crystals are of lower frequency than those emitted by pure crystals. By carefully choosing the doping material, the band structure can be modified in such a way that the emitted photons are visible, and thus they may be useful in scintillation.

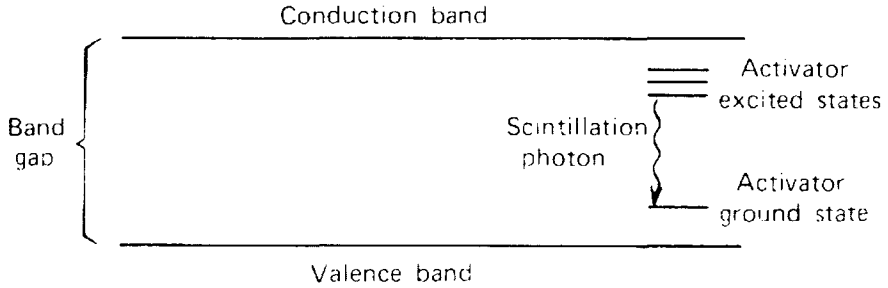

Figure 2.1: Energy band structure of an activated crystalline scintillator [10].

Other forms of inorganic scintillators

Certain silicate glasses, as well as gaseous materials, may also be useful as scintillators. Glasses exhibit relatively low light output, but physical properties such as resistance to corrosion and high temperatures make them useful in applications in which the detector must be subjected to environmental extremes. In addition, they offer the convenience of being available in virtually any shape, ranging from the widely used cylinder to small-radius spheres.

Gaseous scintillators, too, are available in a wide range of shapes, since any container may be chosen. However, the scintillation efficiency exhibited by gases is typically much lower than that observed in glasses, which are themselves quite inefficient. The very low efficiency of gas scintillators results from the wide variety of de-excitation modes available to excited electrons left behind by passing charged particles or radiation. These modes include several which do not result in scintillation, such as intermolecular interaction. De-excitations absent the emission of light are termed *quenching* and generally involve the release of energy as heat. The relatively high probability of quenching processes leaves very little energy to be converted to scintillation light, which leads to low light output. As for the de-excitation processes which result in photon emission, many of these yield ultraviolet photons. This problem could be solved by employing specialised, ultraviolet-sensitive equipment. Alternatively, a second gas could be mixed with the scintillator gas. The second gas absorbs energy from the emitted, high-energy photons, thereby rendering them visible. Despite the inefficiency of light emission, as well as the inconveniently high energy of the emitted photons, the emission processes occur quickly. So quickly, in fact, that gas scintillators are some of the fastest available detectors. Gas scintillators are therefore useful in applications involving high count rates, in which efficiency is not of paramount importance, such as triggering systems.

2.1.2 Organic scintillators

The scintillation process in organic materials is based on the excitation of single molecules. As a result, the emission of scintillation light by organic materials occurs, regardless of the physical state of the material. That is, whether a particular type of scintillating molecule is in the solid, liquid or gaseous state, it exhibits fluorescence. Inorganic crys-

tals, it has been shown, do not share this property. Recall that, in these materials, the scintillation process depends on the crystal lattice structure, since it is the regular lattice spacing which determines the energy band structure.

Organic crystal scintillators

Unlike inorganic crystals, certain organic crystals may be used in their pure forms as scintillators. One important example is anthracene, which has the highest light yield of any organic scintillator. Organic crystals are generally quite fragile and, as a result, only small samples are easily available. This limitation may be important in applications which require a large scintillator volume to increase the observed count rate.

The scintillation efficiency of these materials is dependent on the angle between the trajectory of the ionising particle and the crystal axis. This may severely limit the energy resolution obtainable in applications in which the incident particle trajectory varies significantly, or in which secondary reactions are important.

Organic liquid scintillators

Organic scintillator material may be dissolved in an aromatic solvent, such as benzene or a benzene-toluene combination, to obtain a liquid scintillator. These liquids are available in large quantities, which may make them the most cost-effective option in applications which require very large scintillator volumes – up to several cubic metres.

Liquid scintillators should be packed in a vacuum-sealed container, in order to avoid the dissolving of oxygen in the solution. Dissolved oxygen can cause quenching, which reduces scintillation efficiency.

In certain applications, in which the activity of a single source is to be measured, it is possible to dissolve the radioactive material in a liquid scintillator. This ensures that 100% of the radiation travels through the scintillator, without first having to penetrate the container walls. This situation has a clear advantage over other scintillator-source configurations, in terms of the increased scintillation efficiency. In fact, the activity of some high energy beta emitters, such as ^{32}P, can be counted with an efficiency of nearly 100%. Lower energy beta emitters generally have a lower associated counting efficiency.

For example, the activity of tritium can be counted with an efficiency of approximately 30%.

Plastic scintillators

Plastic scintillators are produced by polymerising scintillator solutions to form solids. These materials may be the most viable choice for applications which require a large-volume, solid scintillator, which is why a plastic scintillator is used in the paddle detectors of the K600 magnetic spectrometer. Plastics have been found to be very useful in radiation detection, due to their cheapness and the ease with which they can be produced. NE102 is one of the most commonly plastic scintillators, with a light output of 65% of that of anthracene, and a peak emission wavelength of 423 nm [10]. Of all the scintillator materials reviewed thus far, plastic scintillators are among the cheapest and most readily available. For these reasons, NE102 will be tested for use in a beam loss monitor.

2.2 Photomultiplier tubes

The use of scintillation as a basis for radiation detection necessitates, in addition to a scintillator, a device which is capable of converting scintillation light to an electric current. A photomultiplier (PM) tube is such a device. PM tubes are highly sensitive, being able to convert a pulse of fewer than a thousand photons to a measurable electrical signal without introducing excessive noise[1].

Figure 2.2 shows the basic elements of the PM tube, and illustrates its operation. Though this figure depicts a PM tube coupled to a scintillator, and though the present work will focus on the use of PM tubes in conjunction with scintillators, it is noteworthy that the uses of PM tubes are many and varied, often in applications which do not involve scintillators. Furthermore, while the figure indicates that a photon is incident on the scintillator, the operating principles of the PM tube are unchanged in situations involving other incident particles, such as the protons used at iThemba LABS.

As shown in Figure 2.2, the first element of the PM tube is a photocathode. This is followed by the electron-optical input system, indicated in the figure as a focusing

[1]Noise is used to indicate random variations in the signal.

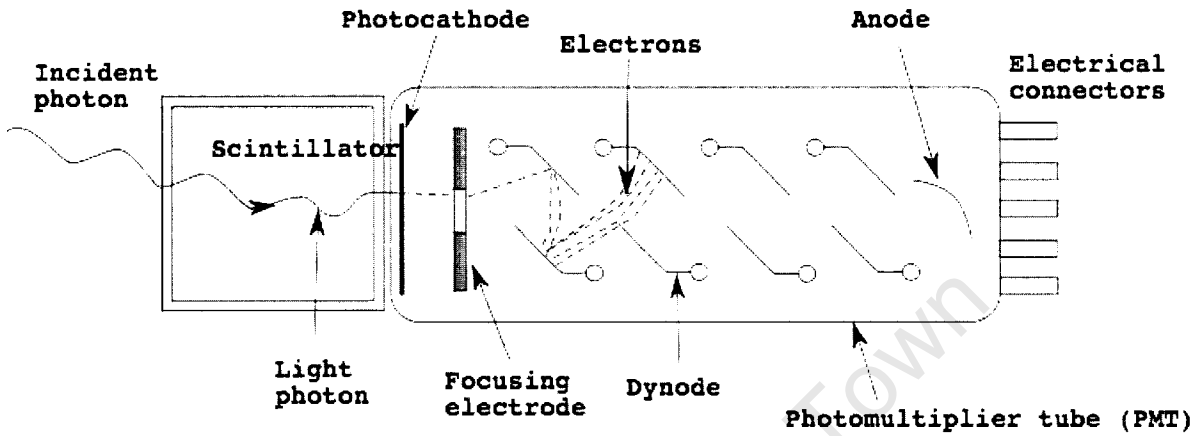

Figure 2.2: Schematic diagram of a photomultiplier tube. By C. Eberhardt and A. Horvath. This work is in the public domain. See `http://en.wikipedia.org/wiki/Image:Photomultipliertube.svg`.

electrode. Next, the dynodes comprise the electron-multiplier system. Finally, there is an anode. What follows is a treatment of the basic elements and of their operation.

2.2.1 Photocathode

When photons strike the photocathode, it emits electrons into the PM tube. This emission occurs by the photoelectric effect, a phenomenon which Einstein explained in his Nobel prize-winning work of 1905 [4]. He discovered the following relationship:

$$E = h\nu - \phi. \tag{2.1}$$

where E is the emitted electron's kinetic energy, h is Planck's constant, ν is the frequency of the incident photon and ϕ is the work function of the metal. Clearly, the minimum photon frequency required for electron emission is $\nu_{\min} = \phi/h$. For frequencies above $\nu_{\min}$, electron emission is possible, but not guaranteed. The probability of electron emission is measured by using a quantity called the *quantum efficiency*, η, which is usually expressed as a function of wavelength:

$$\eta(\lambda) = n_e/n_\gamma, \tag{2.2}$$

where n_γ is the number of incident photons and n_e is the number of emitted electrons. Photocathodes vary greatly in their characteristics, notably in peak response wavelength and maximum quantum efficiency (see Table A.1). The most efficient photocathodes are made from semiconductors and have peak quantum efficiencies close to 30%. The choice of photocathode should be determined by the wavelength of the application and the required quantum efficiency.

2.2.2 Electron-optical input system

Electrons, having been ejected by the photocathode, must be directed toward the electron multiplier system. This is accomplished by the electron-optical input system. In most PM tubes, as shown in Figure 2.2, this system comprises a focusing electrode. In some of the more rare designs, magnetic fields are used, with or without electric fields. Whether the system consists simply of one electrode, or a complicated array of electrodes and electromagnets, it must satisfy some basic requirements. Of course, the system should be as efficient as possible. That is, as many photoelectrons as possible should be directed to the electron multiplier system. In addition, the time taken by a photoelectron to reach the electron multiplier should ideally be independent of the point from which it was emitted by the photocathode. This is accomplished by carefully choosing the electric field configuration set up by the input system. Figure 2.3 shows the electric field lines and equipotential surfaces in a typical electron-optical input system.

2.2.3 Electron multiplier system

The heart of the PM tube is the electron multiplier system, which consists of an array of electrodes, called dynodes. Photoelectrons are focused on the first stage of the multiplier by the electron-optical input system. The dynode then emits electrons via secondary emission. These secondary electrons are accelerated toward the second stage, on which they impinge, thereby causing further secondary emission. This process continues through the series of dynodes. The result is a stage-wise increasing cascade of electrons, which is finally showered onto the anode, with an intensity of up to 10^7 times that of the original trickle of photoelectrons.

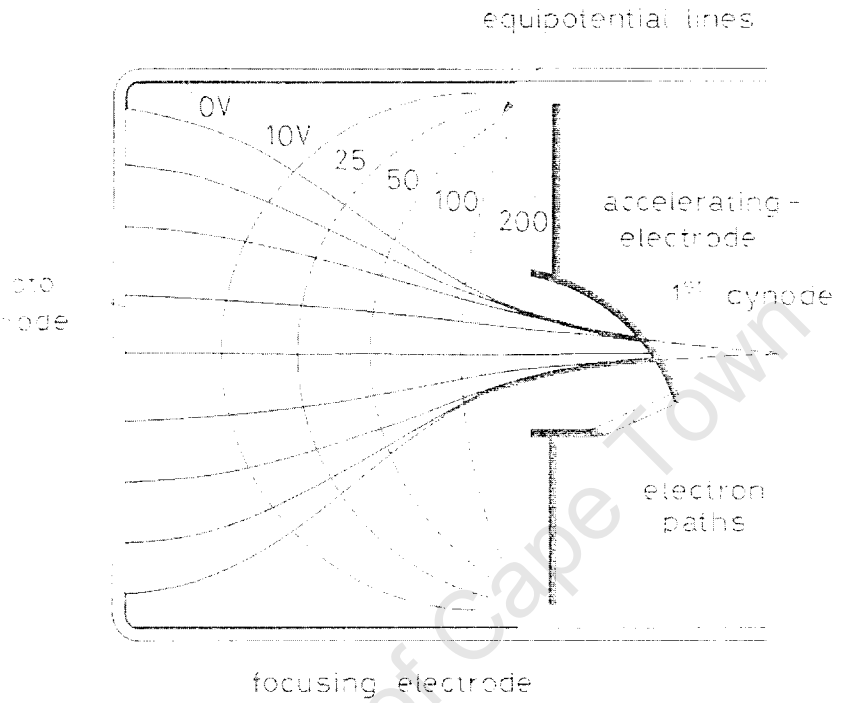

Figure 2.3: Electric field configuration in electron-optical input system [11].

Secondary emission is similar in principle to the photoelectric effect, except that the incident particles are electrons. An accelerated electron penetrates the surface of a dynode, exciting other electrons within the material. Of these electrons, some have sufficient energy to migrate towards the surface. A fraction of those which reach the surface have sufficient energy to escape, and these are emitted as secondary electrons.

The gain produced by each dynode is called the *secondary emission factor*, $\delta(E)$, given by

$$\delta(E) = \frac{n_{se}(E)}{n_{pi}}. \tag{2.3}$$

where n_{pi} is the number of primary incident electrons, n_{se} is the number of secondary emitted electrons and E is the incident electron energy. $\delta(E)$ is highly dependent on E, due to two competing factors. At low incident electron energies, electrons within the dynode will only be slightly excited, and very few will reach the surface for subsequent emission. At much higher incident electron energies, many electrons will be highly

excited, but more of these excitations will occur deep within the volume of the dynode, since the incident electron would be more penetrative. At greater depths within the dynode, even moderately excited electrons may not reach the surface, since they have to travel through so much material. At some optimal incident electron energy, a balance is struck between having sufficient energy to adequately excite secondary electrons and ensuring that excitations do not occur at such depths that secondary electrons cannot reach the surface. At such optimal energies, which are material-dependent, maximum secondary emission can be achieved.

The first stage of the electron multiplying system is held at a higher electric potential than the photocathode. Each subsequent stage is in turn at a higher potential than the previous stage. The increase of potential from stage to stage ensures that the photoelectrons and, later, the secondary emitted electrons are properly directed through the multiplying system.

2.2.4 Anode

The last element in the PM tube, the anode, conducts electrons to an external circuit. Secondary electrons emitted by the final stage of the multiplier system are accelerated toward the anode, due to the voltage difference. In designing the PM tube, it is critically important that the anode be maintained at a sufficiently high voltage, relative to the final diode, so as to ensure that the secondary electrons are efficiently collected. If the voltage is too low, *space charge* effects may occur, whereby secondary electrons build up near the anode, reducing the intensity of the electric field and adversely affecting the collected current [6].

2.3 Photodiodes

Photomultiplier tubes have become the *de facto* standard for the conversion of light pulses to electrical signals. However, due to their high cost and typically extensive size, they are not practical for use in applications which require many detectors to be distributed around larger, more complex apparatus.

It was reported as early as the 1960s [1,8] that the light-sensitivity of photodiodes could be exploited in scintillation applications. That is, a photodiode could be coupled to a scintillator, and used to convert the scintillation light to electrical signals. Dousse and Rhême showed that a photodiode could be used directly as an α detector [3].

Due to their low price and compact size, the use of photodiodes in beam loss monitors is promising. A comprehensive treatment of semiconductors is beyond the scope of this work, and can be found in any text on solid state physics. The interested reader is referred to [9]. However, the choice of an appropriate photodiode requires an understanding of semiconductors, and for this reason a brief explanation of their properties is included here.

2.3.1 Semiconductor properties

A semiconductor is a solid material, the electrical conductivity of which places it between an insulator and a conductor. The use of semiconductors has become essential in electronic devices, precisely because their electrical properties can be modified by the controlled addition of impurities. See the introduction to doping in §2.1.1.

The energy band structure, which was introduced in §2.1.1, can be used to explain the conductivity of a material. Insulators have large band gaps: thus at room temperature, most electrons are in the valence (lower) band, because their thermal energy is insufficient to excite them to the conduction (higher) band. The valence electrons are essentially bound to atoms. This explains the fact that, when an electric field is applied to an insulator, currents typically do not flow. In a conductor, however, there is no gap between the valence and conduction bands. Electrons are essentially free to move throughout the material, and currents flow when an electric field is applied to a conductor. A semiconductor, as the name suggests, is an intermediate case. The band gap is present, but small enough that thermally excited electrons can be found in the conduction band, available to flow as current under the action of an applied electric field.

Valence electrons in a semiconductor crystal may occasionally acquire sufficient thermal energy to break their covalent bonds and transit the band gap and enter the conduction band. Such electrons leave *holes* in the crystal lattice, forming electron-hole pairs. A hole has the important property of behaving like a positive charge carrier. Consider,

for example, an electron at a lattice site adjacent to a hole. If the electron breaks its bond and moves to fill the hole, thus creating a new hole, then the original hole appears to have moved to the electron's position. In summary, the motion of an electron in one direction is equivalent to the motion of a hole in the opposite direction. This is consistent with the motion of a positive charge carrier in an electric field, as compared to that of a negative carrier.

A semiconductor's conductivity, σ, as well as the current density, J, under an applied electric field, E, can be calculated by considering the charge carriers – the electrons and holes. The first quantity required for this calculation is the electron concentration, n_i. In pure crystals, this is also the hole concentration, since they contain equal numbers of electrons and holes. It should be noted that n_i is the concentration in a state of *equilibrium*, in which the rate of electron-hole generation is equal to the rate of electron-hole recombination. The excitation of electrons from the valence to the conduction band requires sufficient thermal energy, therefore the electron-hole concentration depends on temperature. From Fermi-Dirac statistics, it can be shown [11] that n_i is given by

$$n_i = AT^{3/2}\mathrm{e}^{-E_g/2kT}, \tag{2.4}$$

where A is a constant, T is the absolute temperature, E_g is the band gap and k is the Boltzmann constant.

The drift velocity of the electrons and holes in a semiconductor, accelerated in an electric field depends on the field strength and the ease with which they can move through the material. The latter is a property of the material, called *mobility*.

$$v_{e,h} = \mu_{e,h}E, \tag{2.5}$$

where v is the drift velocity, μ is the mobility, and the e and h indices indicate that equation (2.5) holds for electrons as well as for holes. The electron and hole mobilities of silicon and germanium are shown in Table A.2. The current density, J, is given by

$$\begin{aligned} J &= \rho v \\ &= q_e n_i(\mu_e + \mu_h)E, \end{aligned} \tag{2.6}$$

where ρ is the charge density and q_e is the electron charge. Equation (2.5) has been substituted for v and the current contributions from electrons and holes have been summed. The conductivity, σ, is obtained from $J = \sigma E$ and equation (2.6):

$$\sigma = q_e n_i(\mu_e + \mu_h). \tag{2.7}$$

2.3.2 Doping in semiconductors

As mentioned above, pure crystals in thermal equilibrium contain equal concentrations of conduction electrons and holes. The relative concentrations can be altered by doping. Dopants used in a particular semiconductor are made of atoms which have either one more or one fewer valence electron in the outermost shell than do the atoms of the pure crystal.

If the atoms of the dopant have one more valence electron, they are called *donor impurities*. Donor impurities modify the band structure, creating energy levels in the band gap which are very close to the conduction band. The additional electrons cannot reside in the valence band, since there are no available states. Instead, they exist in the newly created states within the band gap. Since these energy levels are close to the conduction band, the excess electrons can, via thermal excitation, become conduction electrons. This represents an increase in conduction electron concentration. Some of the excess electrons will, instead of entering the conduction band, fill naturally occurring holes in the valence band, which decreases the hole concentration. These processes result in the electrons being the majority charge carriers. Semiconductors which have been doped with donor impurities are called *n-type* semiconductors.

Alternatively, if the atoms of the dopant have one fewer valence electron, they are called *acceptor impurities*. Like their donor counterparts, acceptor impurities distort the band structure. However, in the case of acceptors, the energy levels created in the band gap are close to the valence band. Since these impurities have one fewer electron, there appears to be an excess hole at the lattice site, which increases the hole concentration as compared to a pure crystal. In addition, since the states created by the impurities are close to the valence band, valence electrons are readily excited into them, which results in an even greater excess of holes. Having been doped with acceptor impurities,

and with holes being the majority charge carriers, these materials are called *p-type* semiconductors.

In practice, crystals are never completely pure, and they always contain both donor and acceptor impurities. Excess electrons will tend to be captured by excess holes, and thus it is the net number of electrons and holes which determines whether a material is n-type or p-type. If a crystal happens to contain equal concentrations of donor and acceptor impurities, it is termed a *compensated* or an *i-type* material.

2.3.3 p-n junction

A p-n junction is the interface between two semiconductors of type p and n, which are in very close contact. There are several ways to form a junction, one of which is to diffuse impurities of one type (say p-type) through one end of a block of the other type (n-type). Figure 2.4a shows a schematic diagram of an np junction, at the instant of

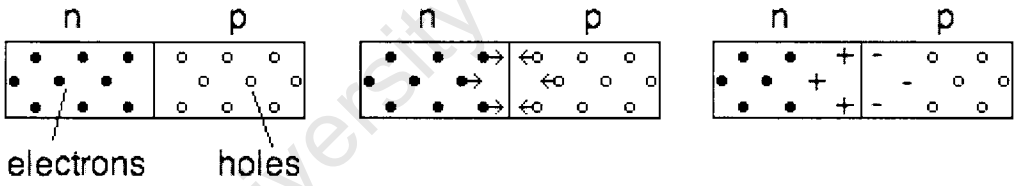

(a) Newly formed np junction. **(b)** Diffusion of electrons and holes. **(c)** Charge build-up near boundary forms depletion zone.

Figure 2.4: Schematic representation of depletion zone formation in an np junction.

formation. The n-type and p-type regions contain high concentrations of electrons and holes, respectively. After formation, the electrons tend to diffuse into the p-type region, while the holes tend towards the n-type region (see Figure 2.4b). The diffusing electrons combine with holes in the p-region, while the diffusing holes capture electrons in the n-region. This results in a build-up of charge around the boundary between the regions, since both regions were electrically neutral before diffusion. A net positive charge has developed on the n-side of the boundary, since the n-region has lost electrons. Similarly, the gaining of electrons by the p-region has resulted in the formation of a region of net negative charge near the boundary, as illustrated in Figure 2.4c.

The charge build-up sets up an electric field gradient across the junction. As more charge builds up, the magnitude of the electric field increases until it is sufficient to prevent further diffusion and an equilibrium is established. The potential difference across the charged region is called the *contact potential*.

The charged region is also known as the *depletion zone*. Mobile charges cannot remain in the depletion zone, as they are immediately accelerated out of the zone by the electric field. This property of semiconductor junctions is exploited in radiation detection. Ionising radiation which passes through the depletion zone will create electron-hole pairs, which are removed from the zone by the electric field. If the junction is connected to a circuit, a current proportional to the number of generated pairs will be observed.

The width of the depletion zone, also called the *depletion depth*, is typically quite small – of the order of tens of microns. This presents a number of challenges to the use of a semiconductor junction as a detector. Since the depletion zone constitutes the most highly radiation-sensitive volume, a smaller depletion zone results in fewer interactions with the radiation, and therefore, fewer collected charges. Additionally, the capacitance, C, of a depletion zone of cross-sectional area A and depth d is given by

$$C = \epsilon \frac{A}{d}. \tag{2.8}$$

From equation (2.8), it is clear that a small depletion depth results in a large capacitance, which results in a poor signal-to-noise ratio when the junction is used for detection. Finally, the electric field in the depletion zone of a typical junction is generally not of sufficient magnitude to collect charges with adequate efficiency.

These challenges may be addressed by applying a reverse bias voltage across the junction. The voltage effectively widens the depletion zone by attracting electrons and holes, in their respective regions, away from the junction. This effect is illustrated in Figure 2.5. The wider zone represents an increased sensitive volume, which increases the number of electron-hole pairs created by a given energy deposition, and thereby improves the energy resolution of the detector. The increased depletion depth reduces the capacitance presented to external electronics, which improves the noise characteristics. The applied voltage also improves the charge collection efficiency, since it increases the electric field in the depletion zone. The reverse bias voltage cannot be made arbitrarily high. There is a maximum voltage above which the junction will fail, by conducting.

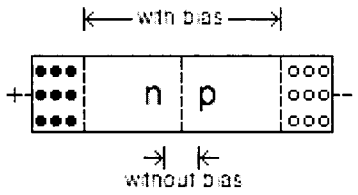

Figure 2.5: The application of a reverse bias voltage increases the depletion depth.

2.3.4 p-i-n photodiodes

p-i-n photodiodes contain an intrinsic layer between the p-type and n-type regions, which results in a wider depletion zone than that found in p-n junctions. The electrical properties of p-i-n diodes differ from those of p-n junctions, largely due to the fact that there is no space charge in the intrinsic layer. This is in contrast to the depletion zones of p-n junctions, which do contain space charge. The absence of space charge in the intrinsic layer of p-i-n diodes results in a nearly uniform electric field within this layer.

2.4 Detector electronics

Even under ideal conditions, including the application of an appropriate reverse bias voltage, the currents generated in a semiconductor detector are too small to be directly usable. The signal must be amplified in order for further processing to be done. Amplification is typically divided into two stages. The first is called *preamplification*, and its purpose is to amplify the weak detector signal and send it to the so-called *main amplifier*. The are many reasons for separating the amplification stages. The preamplifier must be close to the detector, in order to minimise capacitance. However, it is often advantageous to keep the main amplifier at least a few metres from the detector, due to limited space, or perhaps the presence of a large piece of equipment would interfere with the nuclear processes occurring in the experiment [5].

Preamplifiers are available in three basic types. These are the current-sensititve, voltage-sensititve and charge-sensitive models. Current-sensititve preamplifiers are inappropriate for this application, as radiation detectors typically have high impedances,

with which they are not designed to work. The output of a voltage-sensitive preamplifier depends on the capacitance at its input, since the voltage at the input is given by

$$V = \frac{Q}{C_t}, \tag{2.9}$$

where C_t is the total capacitance at the input. Since the capacitance of semiconductor diodes is not stable, but rather varies with temperature, the voltage-sensitive preamplifier is not appropriate for use with the envisioned beam loss monitor. The output of a charge-sensitive preamplifier is independent of the input capacitance, and it is therefore this type which will be used [11].

Commercially available preamplifiers, while possessing excellent noise characteristics, are so expensive that their incorporation into the detector design would be incompatible with the goal of producing a cost-effective system. In order to satisfy this requirement, a simple and inexpensive preamplifier has been designed. The detector electronics, including the photodiode (labelled PD) and the preamplifier, are shown schematically in Figure 2.6. This preamplifier, which will be referred to as the *project preamplifier* is a modified version of an earlier unit designed by R.W. Fearick.

The 100 nF capacitor across the photodiode (labelled C1), as well as the two 10 MΩ resistors were added to the original design. These components act as a low-pass filter, improving the noise characteristics of the system. The operation of low-pass filters will be discussed in detail in § 3.3.

The preamplifier consists of two stages, which were both implemented using AD711JN biFET (Bipolar Field Effect Transistor) operational amplifiers from Analog Devices. These units feature FET inputs which, owing to their high input impedance, provide optimal noise characteristics. The first stage is a modified, active high-pass RC filter, with input capacitance $C_i = 100$ nF and feedback resistance $R_f = 88$ MΩ. A feedback capacitance $C_f = 20$ pF provides noise filtering. The non-inverting input line is grounded.

The second stage has a resistance of 54 kΩ on the inverting input and a feedback resistance of 180 kΩ. This stage amplifies the signal, with a gain of $180/54 \approx 3.33$. The non-inverting input is grounded. The supplies are ± 12 V, and they are decoupled from the circuits via 100 nF capacitors.

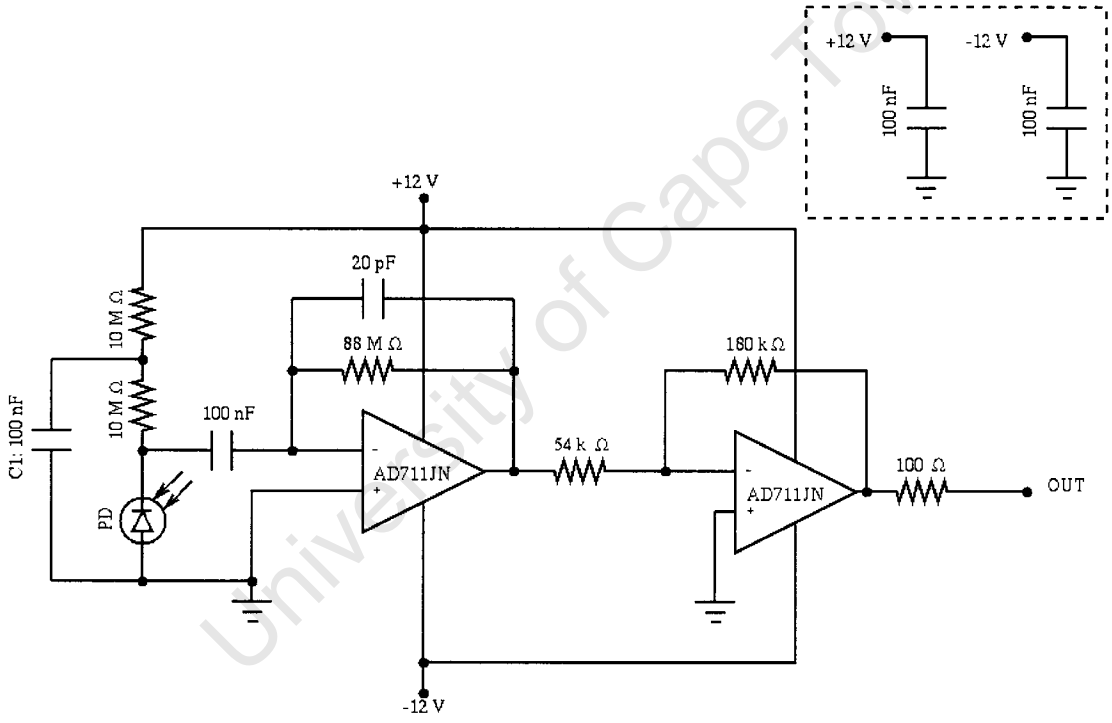

Figure 2.6: Schematic diagram of the detector electronics.

Chapter 3

Beam loss monitors: design tests

After consideration of the advantages and disadvantages of the various radiation detection technologies, it was determined that the design process would be focused on detector systems based on semiconductor photodiodes. This determination was primarily based on the low cost and compact size of these diodes, and it was supported by reports that they can be efficient detectors [3]. This chapter will comprise an outline of the tested detector designs, as well as a presentation of the results obtained from tests carried out at iThemba LABS.

A p-i-n type photodiode was chosen for use in the detector. The p-i-n diode was preferable to the p-n diode, since the i-type region provides a wider depletion zone which, as previously discussed, improves energy resolution and efficiency. Furthermore, the reduced capacitance resulting from the greater depletion depth reduces the noise generated by the detector. A silicon diode was used, rather than germanium, since the application required the detector to function at room temperature. The particular diode model used was the Siemens BPW34[15]. The reasons for choosing this model were its low cost, coupled with its relatively large photosensitive area. Larger photodiodes are available, but cost increases dramatically with area. The Siemens BPW34 has an excellent size to cost ratio.

3.1 Designs

Two types of detectors were tested. The first type, which will be referred to as a *simple photodiode* detector, is a photodiode used directly as a particle detector. In the simple photodiode detector, electron-hole pairs are created within the diode by charged particles, or more specifically, by accelerated protons. The second type, which will be referred to as a *scintillator-photodiode* detector, is a photodiode coupled to a plastic scintillator. In this type of detector, protons penetrate the plastic, causing it to produce pulses of scintillation light. These pulses enter the diode, where the scintillation photons excite electrons within the depletion zone, thereby creating electron-hole pairs. The designs of both detectors are shown schematically in Figure 3.1.

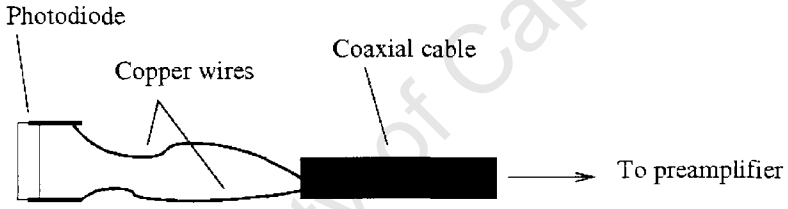

(a) In the simple photodiode detector, a photodiode is used to directly detect charged particles.

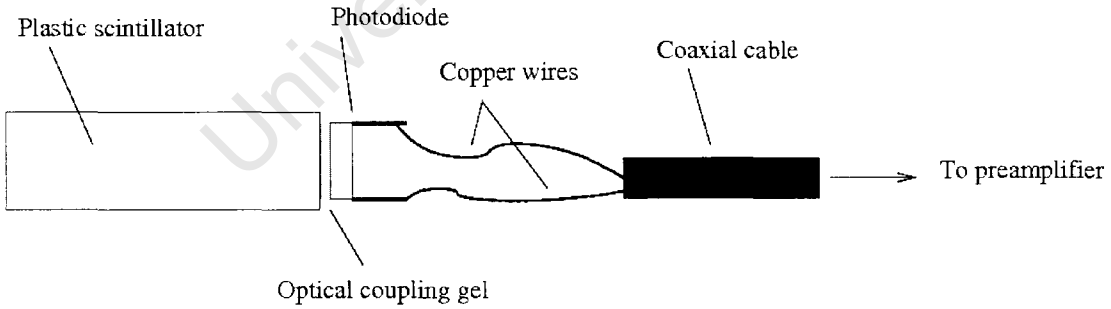

(b) In the scintillator-photodiode detector, a photodiode is used to detect charged particles indirectly by the flashes of light they produce in the plastic scintillator.

Figure 3.1: Schematic diagrams of photodiode and scintillator-photodiode detectors.

The first step in the process of assembling the simple photodiode detector is to solder the terminals of the photodiode to a coaxial cable, which will be used to carry the signals to a preamplifier. At this stage the device should function as a detector. Before it can be used to collect useful data, however, it must be rendered light-tight. This is necessary

because the photodiode is sensitive to visible light, and therefore the signal produced by penetrating protons would be completely overshadowed by that produced by visible photons. Light-proofing is accomplished by wrapping the entire assembly, starting with the diode and extending a few centimetres onto the coaxial cable, in black insulating tape. The effect of light-proofing is illustrated in Figure 3.2. As shown in the diagram,

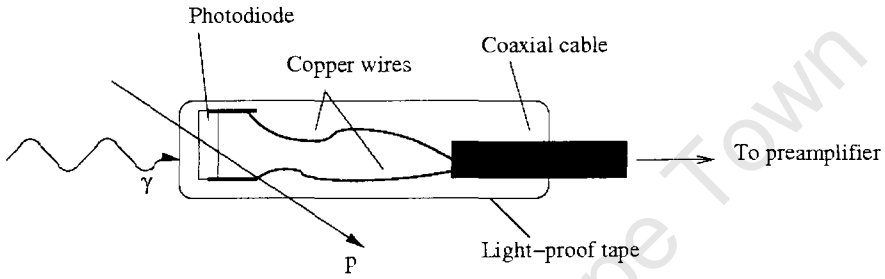

Figure 3.2: Light-proofing is done with black insulation tape. Visible photons are stopped by the tape, but accelerated protons pass through to the photodiode.

the desired effect is that the shielding prevent visible photons from reaching the diode, while allowing high energy protons to pass through. When light-proofing, care must be taken to properly cover any folds in the tape, or sharp corners, which are susceptible to light leakage. Once this process is complete, the simple photodiode detector is ready for use.

The assembly of the scintillator-photodiode detector is similar to that of the simple photodiode model, with the addition of the optical coupling process. In order to safeguard detector efficiency, good optical contact between the scintillator and the photodiode must be achieved. To this end, the surface of the scintillator must be polished to eliminate rough patches and imperfections. These would otherwise contribute to unwanted reflections and generally poor optical contact. Before coupling, both surfaces must be cleaned to ensure they are free of dust and oil. An optical coupling gel, based on silicone, is used to facilitate good contact. A small bead of gel is placed at the centre of the surface of the plastic, and the photodiode is slowly pressed against it. As the gel is forced towards the edges, air is pushed out as well. It is important that the joint be free of air bubbles, as these would lower the optical efficiency.

The characteristics of the photodiodes used in this project have been documented by Siemens [15]. The physical dimensions of the plastic scintillator were measured to be

6.00 mm by 5.15 mm by 33.35 mm, using Mitutoyo 'Absolute Digimate' digital Vernier callipers (Part# CD-8"C).

3.2 Tests and results

Several design tests were carried out at iThemba LABS between October 2006 and September 2007. The methods and results of these experiments will be described in this section. It should be noted that the lack of data for plastic scintillator detectors is unavoidable, since the pulses yielded by these detectors were found to be too small to be usable.

3.2.1 Initial experiment

The purpose of the initial experiment was to determine whether the detector systems would respond to radiation.

The detectors were placed in the spectrometer vault, near the beam line, where there was thought to be a high proton flux. Figure 3.3 shows a schematic representation of the experimental setup, in the case of a single detector. Ortec 142A preamplifiers were connected to the detectors using 50 Ω coaxial cables. Care was taken to mount the preamplifiers close to the detectors, so as to minimise cable capacitance and thus improve the noise characteristics of the detector system. The preamplifiers were connected to the spectrometer vault patch panel, which provides a direct connection to the data room.

In the data room, the preamplifiers were connected to spectroscopy amplifiers, which would be used to amplify and shape the pulses. Finally, the amplifiers were connected to an oscilloscope for signal observation and saving.

Test pulse generators were connected, via the patch panel system, to the preamplifiers. These were used to simulate proton events, in order to ensure that the electronics were functioning properly. One such test pulse, after processing by one of the preamplifiers, is shown in Figure 3.4. This pulse was measured directly from the preamplifier, without being processed by the spectroscopy amplifier. This pulse has the expected shape, and thus the setup was deemed functional. Pulses associated with real events,

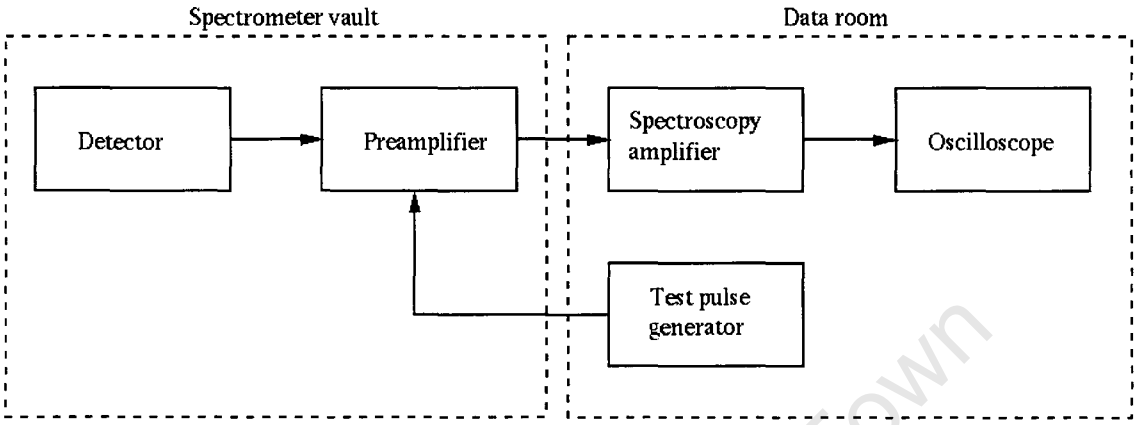

Figure 3.3: Schematic representation of initial experimental setup.

that is, pulses due to proton interactions, were not observed during the initial experiment.

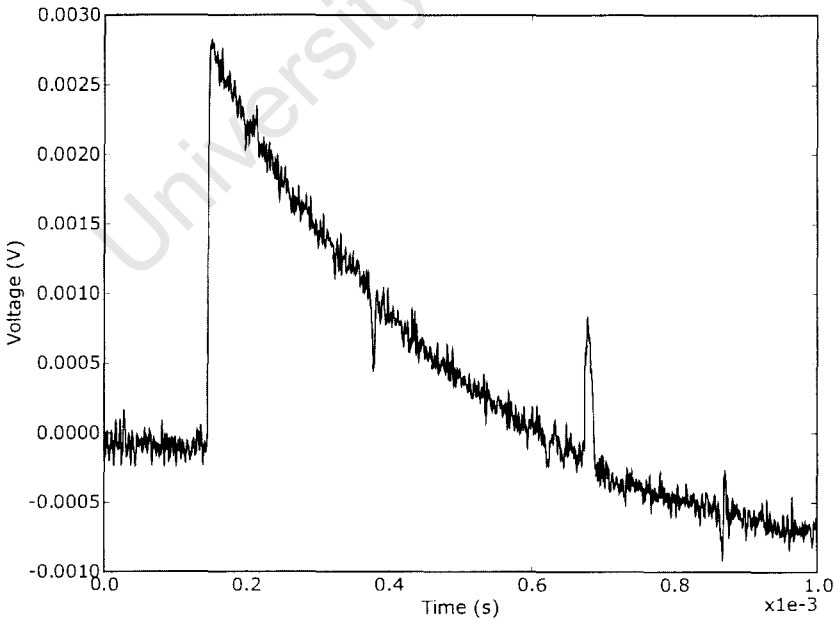

Figure 3.4: This test pulse originated in the pulse generator. It was sent through the preamplifier and returned to the oscilloscope.

3.2.2 ^{90}Sr experiment

Following the failure to detect real pulses during the initial experiment, it was decided that it would be useful to perform an experiment with a radioactive source. In this way the experimental conditions could be more easily adjusted, compared to when the detector was placed in the spectrometer vault. For safety reasons, the vault could only be accessed when the beam was not present, which often meant waiting for several hours before adjustments to the detector could be made.

In the present experiment, a simple diode detector was placed in the vicinity of a ^{90}Sr source. The electronics were set up as in the initial experiment, without the use of the patch panel system. This experiment did not make use of a test pulse generator. The experimental setup is shown in Figure 3.5.

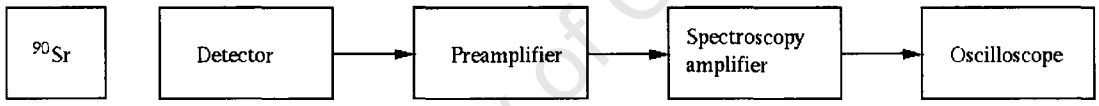

Figure 3.5: Logical representation of the experimental setup in the ^{90}Sr experiment.

During the course of this experiment, it was determined that the magnitude of the signal observed on the oscilloscope was strongly dependent on the proximity of the photodiode to other objects, such as an experimenter's hand. It was postulated that this effect could have been due to capacitative coupling of the detector to a nearby signal. The photodiode was shielded with aluminium foil in order to counteract this effect.

^{90}Sr is a pure beta minus (β^-) source [10]. That is, β^- is the sole mode by which ^{90}Sr decays. The reaction, shown in equation (3.1), involves the conversion of a ^{90}Sr nucleus to a ^{90}Y nucleus, via the emission of a 0.546 MeV beta electron and an electron-type antineutrino.

$$^{90}\mathrm{Sr} \rightarrow {}^{90}\mathrm{Y} + e^- + \bar{\nu}_e \tag{3.1}$$

Neutrinos have virtually no cross-section for interaction with matter, so they most often go undetected. The fast beta electrons, however, have a much larger interaction

cross-section and thus they are expected to be detectable with the photodiode detector. Figure 3.6 shows a typical pulse, which was processed by the spectroscopy amplifier.

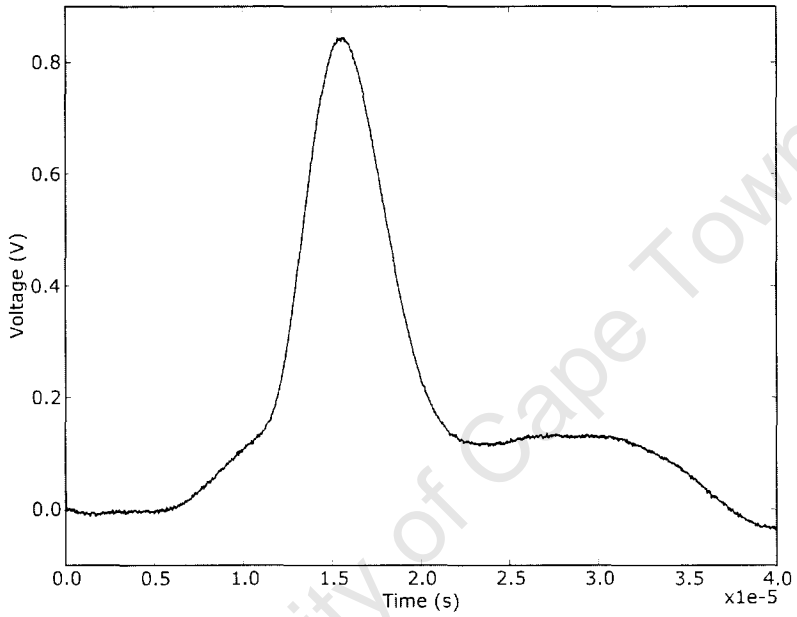

Figure 3.6: Detected β^- particle from ^{90}Sr source.

The effect of applying a reverse bias voltage across a junction was examined. Figure 3.7 shows pulses from ^{90}Sr, with and without an applied reverse bias voltage.

The detector system was observed to be vulnerable to electronic pickup. This is illustrated in Figure 3.8, wherein a signal with a period of approximately 0.01 s can be seen. This corresponds to a frequency of 100 Hz.

3.2.3 Diode-diode coincidence experiment

In the coincidence experiment performed at iThemba LABS, two diodes were mounted face-to-face, as shown in Figure 3.9. In this configuration, protons travelling within a certain solid angle could possibly trigger both detectors. The advantage of coincidence measuring is an increased probability that observed pulses represent real events. Independently, the detector systems may respond to external effects in such a way as to

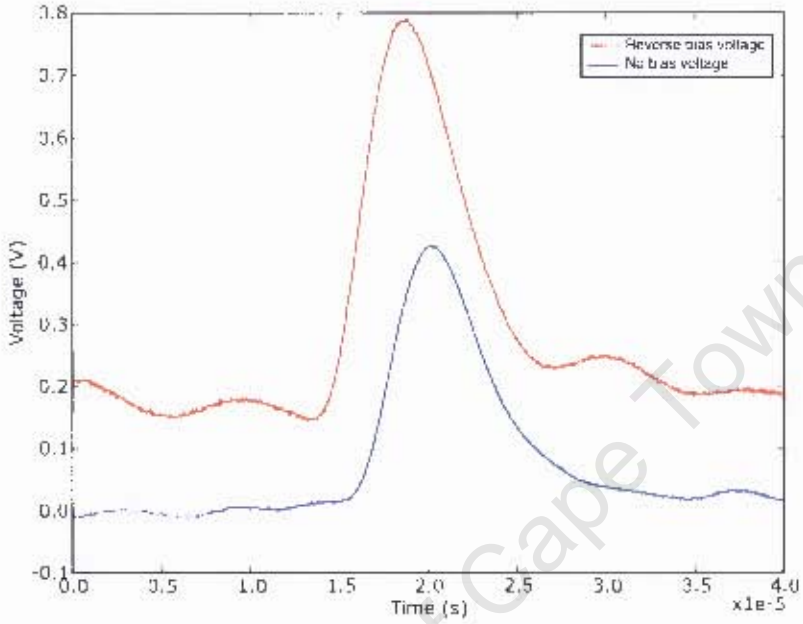

Figure 3.7: The effect of an applied reverse bias voltage of 15 V.

falsely indicate an event. However, the likelihood of obtaining a false positive for both detectors simultaneously is quite remote. Therefore, additional electronics were installed in order to measure coinciding pulses.

Figure 3.10 shows the electronic setup of the coincidence experiment. Just as in the initial experiment, the detectors are mounted on the beam line and connected to closely placed preamplifiers. Again, the preamplifiers are connected to spectroscopy amplifiers via the patch panel system. The signals from each amplifier, in addition to being routed to the oscilloscope, are also sent through a *timing SCA* (single channel analyser). A timing SCA takes a pulse as input, and outputs a square pulse if the height of the input pulse falls within a certain range. The selection of this range can be made so as to disregard lower pulse heights, in the region dominated by noise. The sum of the signals from the two SCA units is fed into a *discriminator*. The discriminator determines whether the two signals contain coincident pulses by measuring the height of the summed signal. If this height is above a critical level, the pulses are deemed to be coincident. The signal then passes from the discriminator to a logical *AND gate*. The AND gate ensures that both detectors sent a signal. This stage rules out situations wherein one

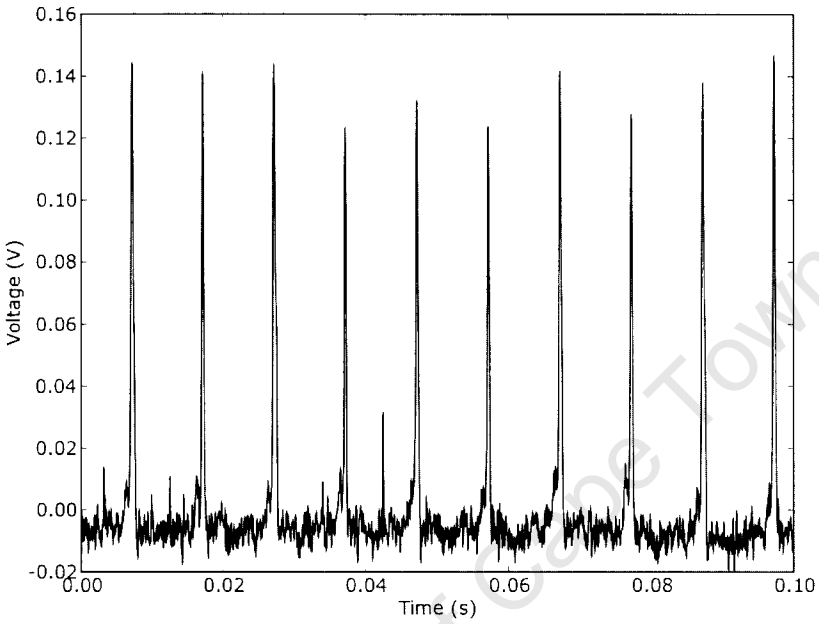

Figure 3.8: 100 Hz background signal.

detector sends a pulse which is large enough to satisfy the discriminator, while the other detector sends nothing. Having passed through the AND gate to the oscilloscope, the pulses should be coincident, and of sufficient amplitude to stand well above the noise.

The results obtained in the coincidence experiment were not surprising. The coincidence count rate was significantly lower than the count rate on either individual detector. This was to be expected, since the protons can pass through the junction depletion zones via many different trajectories, yet only a fraction of these will pass through both diodes. Despite the lower count rate, the increase reliability with which a coincident pulse can be attributed to a particular source is valuable in and of itself.

Figure 3.11 shows typical examples of coincident pulses. Here, the red and blue lines represent the two detectors. Figure 3.11a illustrates a common situation, in which one pulse was measured coincidentally, while two others passed through single detectors. Figure 3.11b shows two pairs of pulses. Interestingly, one particle appears to have deposited more energy in the blue detector than in the red detector, while the other appears to have done just the opposite. This could be construed as counterintuitive,

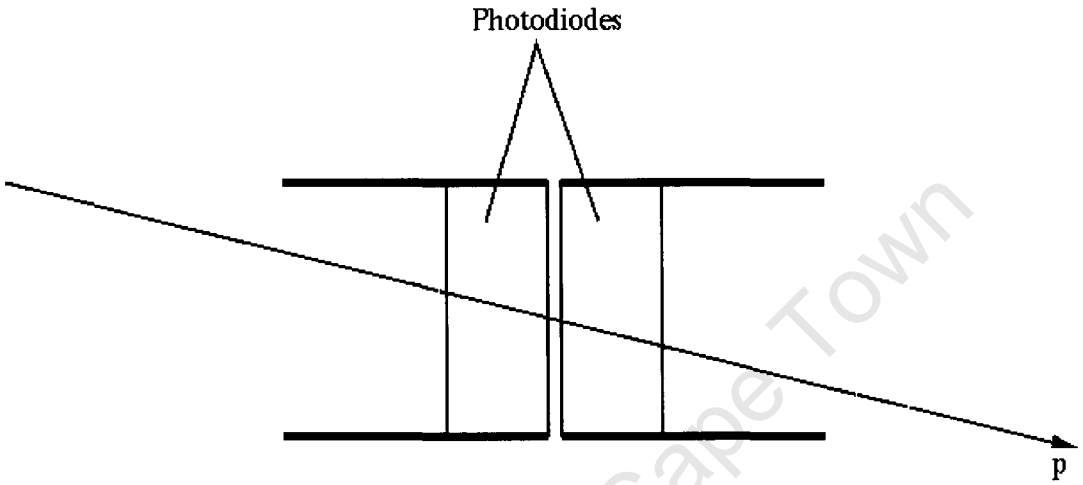

Figure 3.9: Photodiodes mounted face-to-face. Passing proton triggers both detectors.

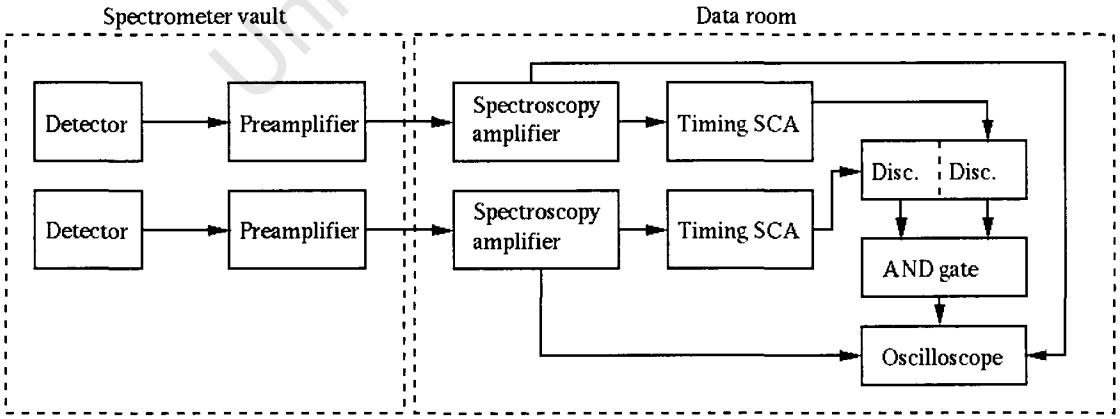

Figure 3.10: Schematic representation of the coincidence measurement experiment.

since one might expect a proton to deposit slightly less energy in the first detector than it does in the second detector. One possible explanation for shift in pulse height order is related to the proton scattering angle. Some scattering angles yield longer path lengths through the first detector than the second, while for other scattering angles, the reverse is true. Figure 3.11c, too, shows two sets of coincident pulses. The first particle appears to have deposited a large amount of energy in one detector, while leaving a much smaller amount in the other detector. The second particle appears to have deposited similar amounts of energy in both detectors.

3.2.4 Preamplifier comparison

A few spectra were recorded at iThemba LABS in order to compare the performance of the project preamplifier to that of the Ortec model. Diode detectors were placed in the vault, using the same electronic setup as the initial experiment. Figure 3.12 shows one spectrum from each preamplifier. The Ortec spectrum in Figure 3.12a shows one large peak on top of a small, periodic background. The signal is relatively clean. Figure 3.12b shows a more noisy signal, as evidenced by high-frequency variation. In addition, there is a pickup frequency, of approximately 1 kHz, on the signal. The source of this frequency was not determined. It is noteworthy that the two preamplifiers were placed in the same area during the experiment. That the project preamplifier was the only one to suffer from the pickup would suggest that it is inferior in terms of shielding.

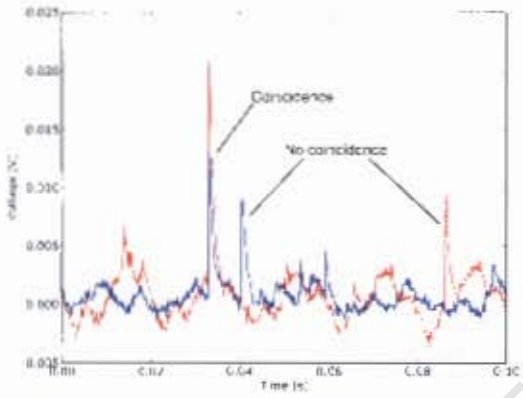

(a) Large pulse measured in coincidence. Other pulses measured by single detector.

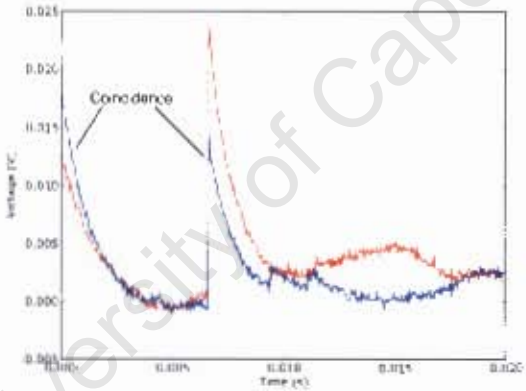

(b) Two pulses measured in coincidence.

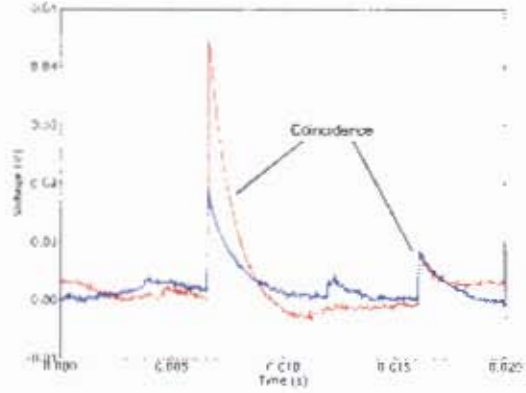

(c) Two pulses measured in coincidence, showing differing energy deposits. One smaller pulse measured on blue channel only.

Figure 3.11: The measurement of coincident pulses yields increased confidence in the identification of legitimate events.

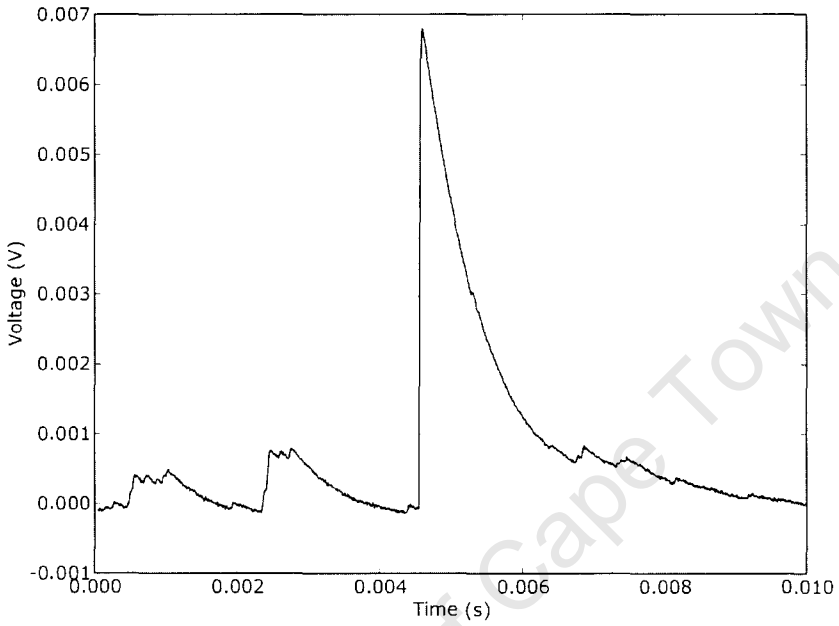

(a) Ortec 142B preamplifier. This signal is clean, with a small periodic background.

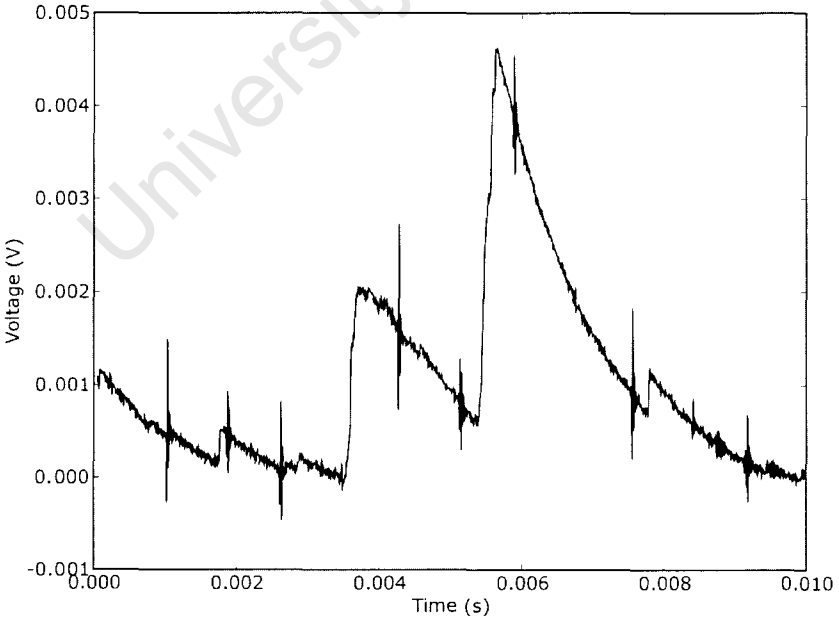

(b) Project preamplifier. This signal is more noisy. It also contains a pickup frequency of 1 kHz.

Figure 3.12: A comparison of the signals measured by the Ortec 142B preamplifier to those measured by the project preamplifier.

3.3 Signal processing

The signals received from the preamplifiers were found to be quite noisy, and therefore some type of filtering was desirable. Noise is typically characterised by high frequency components superimposed on the lower frequency signal, and thus an appropriate filter will attenuate high frequency compontents, while letting low frequency components pass unaffected [16]. Such a filter is called a *low-pass* filter. Here, the terms "low" and "high" are relative to the *cutoff frequency* of the filter, which is defined below.

3.3.1 RC low-pass filter

A simple analog low-pass filter can be realised by an RC series circuit, as shown in Figure 3.13. The basis of operation of the RC low-pass filter is the fact that the

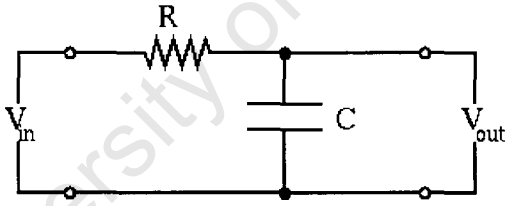

Figure 3.13: An RC series circuit functioning as a low-pass filter.

capacitor does not react instantaneously to changes in the input voltage, V_{in}. When the input voltage is increased (or decreased), the capacitor charges (or discharges), altering the output voltage, V_{out}. The finite time taken by the capacitor to charge or discharge results in a phase difference between the input and output voltages. The higher the frequency of the input voltage, that is, the faster the input voltage changes, the less time the capacitor has to respond, and therefore the greater the attenuation.

The behaviour of the filter may be characterised by its *time constant*, τ. In the case of an RC filter, the time constant is determined by the values of the resistance and capacitance:

$$\tau = RC. \tag{3.2}$$

An elementary analysis of the RC series circuit with constant input voltage shows that the charge, Q, on a capacitor which has been charging for time, t, is given by

$$Q(t) = CV_{in}\left[1 - \mathrm{e}^{-t/RC}\right]. \tag{3.3}$$

From equation (3.3), it is clear that the time constant is a measure of the characteristic time taken by the capacitor to accumulate charge. For example, when $t = RC$, the capacitor has accumulated a fraction $(1 - \mathrm{e}^{-1}) \approx 63\%$ of the maximum charge.

Returning to the RC low-pass filter, the time constant determines the cutoff frequency, f_c, as follows:

$$f_c = \frac{1}{2\pi\tau}. \tag{3.4}$$

An ideal low-pass filter will pass frequencies below f_c with zero attenuation, while completely blocking out components of the signal with frequencies greater than f_c. However, real filters fail to discriminate frequencies so precisely. They attenuate a certain band of frequencies below f_c, while passing a certain band above f_c. Figure 3.14 shows the frequency response of a typical low-pass filter, which has been designed to produce a very flat response in the pass band. The horizontal axis shows the input frequency, normalised to the cutoff frequency, on a logarithmic scale. The vertical axis shows the gain in *decibels*, the symbol for which is dB. The decibel is used to logarithmically describe the ratio of two quantities. The gain, g, of a filter is given by the ratio V_{out}/V_{in}. This can be expressed in decibels as follows:

$$g(f) = 10\log\left(\frac{V_{out}}{V_{in}}\right)\ \mathrm{dB} \tag{3.5}$$

For example, the filter illustrated in Figure 3.14 shows a gain of -3.01 dB at $f/f_c = 1$. Substituting this value of the gain into equation (3.5), it becomes clear that $V_{out}/V_{in} \approx 1/2$. That is, the filter has a gain of $1/2$ at the cutoff frequency. The accuracy of a low-pass filter is characterised by the rate of attenuation with increasing frequency. Higher order (more accurate) filters will have a steeper gradient in the stop band than that shown in Figure 3.14, which illustrates a first order filter.

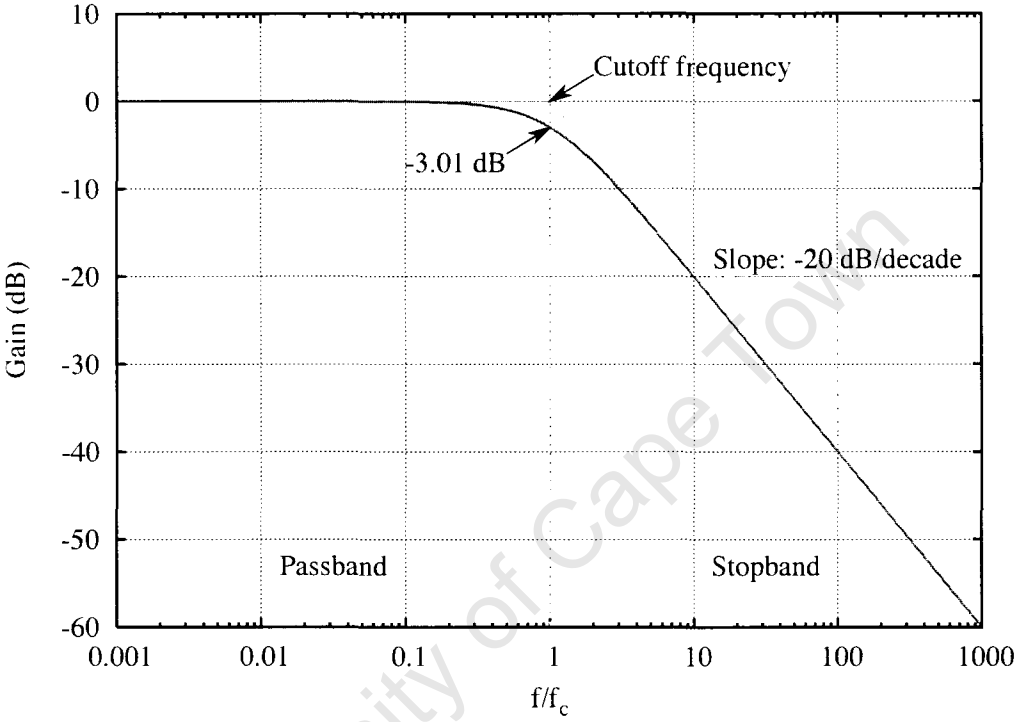

Figure 3.14: Frequency response of a first order low-pass filter. The vertical scale shows gain. The horizontal scale shows the frequency of the input voltage, normalised to the cutoff frequency of the filter. This image was produced using gnuplot and a modified version of the script at `http://en.wikipedia.org/wiki/Image:Butterworth_response.png`. The original script is in the public domain.

Simulating a low-pass filter

An analog low-pass filter, such as the RC filter described above, may be simulated by constructing a digital filter. This is done by discretising the temporal behaviour of the filter. Considering the RC circuit shown in Figure 3.13, the following relationships are obtained:

$$V_{in}(t) = I(t)R + V_{out}(t). \tag{3.6}$$

$$Q(t) = CV_{out}(t), \tag{3.7}$$

where I is the current in the circuit and Q is the charge on the capacitor. Equation (3.6) is obtained from Kirchoff's loop rule, while equation (3.7) follows directly from the definition of capacitance. Recalling that current is the time-deriviative of charge, and noting that the capacitance, C, is constant, equation (3.8) is obtained by differentiating equation (3.7) with respect to time.

$$I(t) = C\frac{\mathrm{d}V_{out}(t)}{\mathrm{d}t}. \tag{3.8}$$

Substituting equation (3.8) into equation (3.6) yields:

$$V_{in}(t) = C\frac{\mathrm{d}V_{out}(t)}{\mathrm{d}t}R + V_{out}(t). \tag{3.9}$$

To discretise this system, assume that the value of $V_{in}(t)$ is sampled at a frequency $f_s = 1/\Delta t$, and that the sampled values form a sequence $v_0, v_1, \ldots, v_N$, such that the temporal order is preserved. This construction can be expressed as follows:

$$v_i = V_{in}(t_0 + i\Delta t) \qquad \forall i \in [0, N]. \tag{3.10}$$

Here t_0 is an arbitrarily chosen time at which sampling begins. Similarly $V_{out}(t)$ is sampled to populate a sequence u_i:

$$u_i = V_{out}(t_0 + i\Delta t) \qquad \forall i \in [0, N]. \tag{3.11}$$

The discrete form of the model may be expressed as:

$$\begin{aligned} v_i &= C\frac{u_i - u_{i-1}}{\Delta t}R + u_i \\ &= u_i\frac{RC}{\Delta t} - u_{i-1}\frac{RC}{\Delta t} + u_i \\ &= u_i\left(1 + \frac{RC}{\Delta t}\right) - u_{i-1}\frac{RC}{\Delta t} \end{aligned}$$

$$
\begin{aligned}
\Rightarrow u_i &= \frac{v_i + u_{i-1}\frac{RC}{\Delta t}}{1 + \frac{RC}{\Delta t}} \\
&= v_i \left(\frac{1}{1 + \frac{RC}{\Delta t}} \right) + u_{i-1} \left(\frac{\frac{RC}{\Delta t}}{1 + \frac{RC}{\Delta t}} \right) \\
&= v_i \left(\frac{\Delta t}{\Delta t + RC} \right) + u_{i-1} \left(\frac{RC}{RC + \Delta t} \right) \\
\Rightarrow u_i &= \alpha v_i + (1 - \alpha) u_{i-1}, \qquad (3.12)
\end{aligned}
$$

where $\alpha = \Delta t/(RC + \Delta t)$ is known as the *filter constant*. Equation (3.12) is the *update equation* of the discrete model. This equation shows how the present output voltage is calculated from the present input voltage and the previous output voltage.

Low-pass filter as an integrator

This RC circuit is also known as an *RC integrating circuit*. To explain the use of this term, equation (3.9) is considered for different values of $\tau = RC$. For large values of τ, equation (3.9) becomes

$$
\begin{aligned}
V_{in}(t) &\simeq \tau \frac{\mathrm{d}V_{out}(t)}{\mathrm{d}t} \\
\Rightarrow V_{out}(t) &\simeq \frac{1}{\tau} \int V_{in}(t)\, \mathrm{d}t, \qquad (3.13)
\end{aligned}
$$

while for small values of τ, equation (3.9) becomes

$$
V_{in}(t) \simeq V_{out}(t). \qquad (3.14)
$$

Equations (3.13) and (3.14) imply that, when the time constant is relatively large in comparison to the pulse width, the pulse will be integrated, and otherwise the pulse will not be affected by the filter.

The z-transform in signal processing

The characteristics of a filter may be easily analysed using the z-transform [22], which is defined as follows. Given a sequence, $x[n]$, the z-transform, $X(z)$, of the sequence is

given by:

$$\mathcal{Z}(x[n]) = X(z) = \sum_{n=-\infty}^{\infty} x[n]z^{-n}. \tag{3.15}$$

In discrete time, *transfer function*, $H(z)$, of a filter is the linear map from the z-transform of the input signal to the z-transform of the output signal:

$$U(z) = H(z)V(z) \Rightarrow H(z) = \frac{U(z)}{V(z)}. \tag{3.16}$$

$H(z)$ for the low-pass filter can be calculated by considering the difference equation of the filter, equation (3.12). Taking the z-transform of all the terms and rearranging yields:

$$\begin{aligned} & U(z) \quad -(1-\alpha)z^{-1}U(z) = \alpha V(z) \\ \Rightarrow \quad & H(z) \quad = \frac{U(z)}{V(z)} = \frac{\alpha}{1-(1-\alpha)z^{-1}}. \end{aligned} \tag{3.17}$$

The filter can now be analysed in terms of the *poles* and *zeros* of the transfer function. The functions $D(z)$ are $N(z)$ are defined as the denominator and numerator of the $H(z)$, respectively. The zeros of the transfer function occur when $N(z) = 0$. At the zeros, the signal is completely attenuated, while at the poles, which occur when $D(z) = 0$, the output signal blows up. Since there are no solutions to $N(z) = 0$ in this case, there are no zeros. There is a pole at $z = 1 - \alpha$.

3.3.2 CR high-pass filter

High-pass filters are similar to low pass filters, except that they attenuate frequency components below the cutoff frequency, while passing higher frequency components. A simple CR series circuit corresponding to a high-pass filter consists of a capacitor and a resistor in series, with the output voltage measured across the resistor. The circuit is shown in Figure 3.15. The cutoff frequency of this filter is identical to that of the low-pass filter, which is shown in equation (3.4). An analysis of the high-pass filter is presented here.

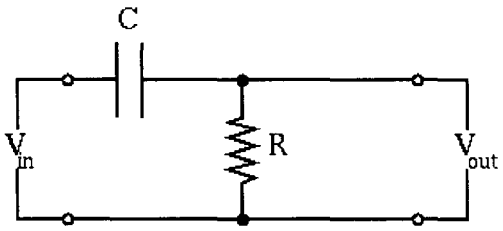

Figure 3.15: An CR series circuit functioning as a high-pass filter.

Kirchoff's loop rule gives us that

$$V_{in}(t) = \frac{Q(t)}{C} + V_{out}(t). \tag{3.18}$$

Recall that the charge, $Q(t)$, on the capacitor is the time-integral of the current, $I(t)$, flowing in the circuit:

$$Q(t) = \int_0^t I(\tilde{t})\,\mathrm{d}\tilde{t}. \tag{3.19}$$

Substituting equation (3.19) into equation (3.18), we obtain:

$$V_{in}(t) = \frac{1}{C}\int_0^t I(\tilde{t})\,\mathrm{d}\tilde{t} + V_{out}(t). \tag{3.20}$$

Noting that $I(t) = V_{out}(t)/R$ and differentiating equation (3.20) with respect to time yields:

$$\frac{\mathrm{d}V_{in}(t)}{\mathrm{d}t} = \frac{1}{RC}V_{out}(t) + \frac{\mathrm{d}V_{out}(t)}{\mathrm{d}t}. \tag{3.21}$$

Discretisation of high-pass filter

The input and output voltages are discretised, as in the previous case, using v for the input and u for the output.

$$\begin{aligned} \frac{v_i - v_{i-1}}{\Delta t} &= \frac{1}{RC}u_i + \frac{u_i - u_{i-1}}{\Delta t} \\ \Rightarrow \frac{1}{\Delta t}(v_i - v_{i-1}) &= \left(\frac{1}{RC} + \frac{1}{\Delta t}\right)u_i - \frac{1}{\Delta t}u_{i-1} \\ \Rightarrow u_i &= \frac{\frac{1}{\Delta t}(v_i - v_{i-1} + u_{i-1})}{\left(\frac{1}{RC} + \frac{1}{\Delta t}\right)} \\ &= \frac{v_i - v_{i-1} + u_{i-1}}{\frac{\Delta t}{RC} + 1} \\ \Rightarrow u_i &= (1-\alpha)(v_i - v_{i-1} + u_{i-1}). \end{aligned} \tag{3.22}$$

where the filter constant α is defined as in the case of the low-pass filter.

High-pass filter as a differentiator

The high-pass filter shown in Figure 3.15 is also known as a *CR differentiating circuit*. Once again, the reason for this is made clear by considering equation (3.21) for different values of $\tau = RC$. If τ is sufficiently small, then equation (3.21) reduces to

$$\frac{\mathrm{d}V_{in}(t)}{\mathrm{d}t} \simeq \frac{1}{\tau}V_{out}(t). \tag{3.23}$$

which shows that, for such values of τ, the output voltage is proportional to the time derivative of the input voltage. However, if τ is sufficiently large, then equation (3.21) becomes

$$\begin{aligned} \frac{\mathrm{d}V_{in}(t)}{\mathrm{d}t} &\simeq \frac{\mathrm{d}V_{out}(t)}{\mathrm{d}t} \\ \Rightarrow V_{in}(t) &\simeq V_{out}(t). \end{aligned} \tag{3.24}$$

In summary, equations (3.23) and (3.24) show that, when the time constant is small in comparison to the pulse width, the pulse will be differentiated, and that when this is not the case, the pulse will pass, unaffectedly, through the filter.

Consider the effect of the differentiating circuit on a step function pulse, as illustrated in Figure 3.16. The step function is transformed into a an exponential tail pulse, with a characteristic decay time determined by the time constant. Mathematically, the

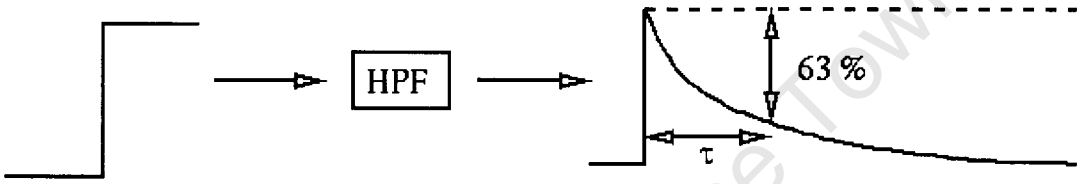

Figure 3.16: CR high-pass filter differentiates a step function. τ is the characteristic time, after which the output has decayed by 63 %.

derivative of the step function is the Dirac delta function [2], $\delta(t)$, given by

$$\delta(t) \equiv \lim_{a \to \infty} \begin{cases} a, & t = 0 \\ 0, & t \neq 0 \end{cases}, \quad \text{where also} \int_{-\infty}^{\infty} \delta(t)\, \mathrm{d}t \equiv 1. \tag{3.25}$$

It should be clear that as $\tau \to 0$, the shape of the output tail pulse approaches that of $\delta(t)$, which is compatible with the above-mentioned finding that the circuit will differentiate the input pulse for sufficiently small values of τ.

3.3.3 Implementation and results

Noise filtering

A digital filter[1] was used to process the experimental data. The filter may be configured in various ways, depending on the desired type of processing. The simplest filtering method is noise filtering, which is achieved by processing the data with a simulated low-pass filter, or RC integration circuit. The data presented in §3.2 have been processed by a chain of successive low-pass filters. The noise levels improve with each iteration,

[1]This was implemented in Python. The source code is listed in Appendix B.

until the improvement from one stage to the next becomes unnoticeable. It was found that five or six runs was generally sufficient. Figure 3.18 shows the effect of the low-pass processing, by comparing the original, unfiltered data to the output.

Pulse shaping

In addition to ordinary noise filtering, it is often desirable to *shape* the pulse into a more convenient form. Pulse shaping has two main purposes in the context of preamplifier pulses. The first is to avoid the *pile-up* effect. Typical preamplifier pulses have long tails which decay rather slowly. If the pulse rate is significantly higher than $1/\tau$, then pulse heights will be distorted due to the lingering tails of previous pulses. Figure 3.17 illustrates the pile-up effect. The pile-up effect is avoided by shaping the pulses to

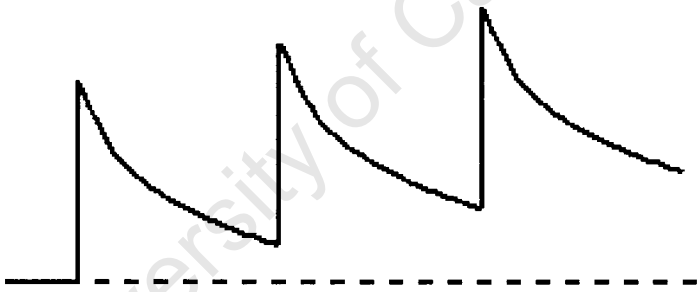

Figure 3.17: Pile-up occurs when the lag between pulses is shorter than the characteristic decay time. Each pulse is shifted up by the height of the tail of the previous pulse.

reduce tail length. In this way, by the time a pulse arrives from the preamplifier, the previous pulse will have decayed sufficiently.

The second purpose of pulse shaping is the improvement of the signal-to-noise ratio. Tail pulses may be unacceptably distorted by typical noise spectra. Gaussian pulses are preferable, due to their resistance to distortion by noise.

Pulse shaping was accomplished by alternatively processing the data with low-pass and high-pass filters. The tail pulses were smoothed out as shown in Figure 3.19.

It should be noted that both the noise filtering and pulse shaping routines produce pulses with heights which differ from those of the input pulses. This is due to the fact

that these routines are set up to control the signal to noise ratio, and not to provide unity gain.

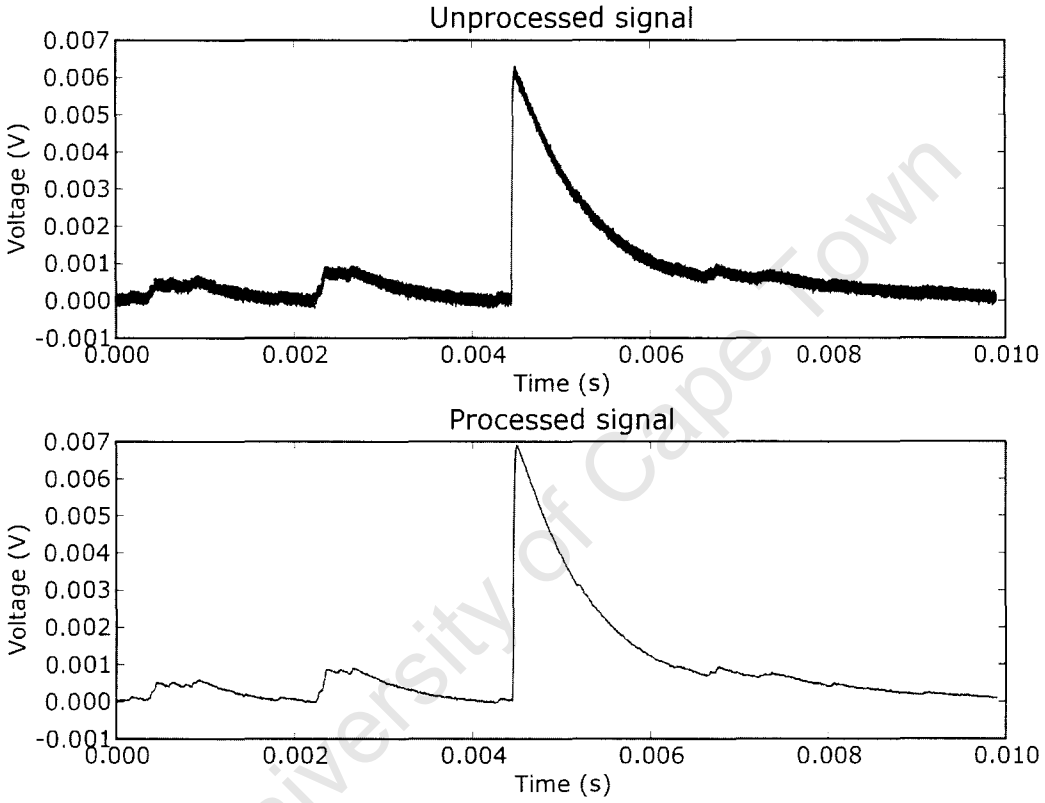

Figure 3.18: The effect of noise filtering. Several runs through a low-pass filter produces a much smoother signal.

Pole zero cancellation

Simple CR-RC filters such as that which is simulated here typically exhibit *undershoot* on the output pulse, which is a result of the relatively long decay time of the preamplifier tail pulse. For sufficiently high count rates, pulses will tend to ride the tails of previous pulses, resulting in distortedly low apparent pulse heights. This effect is similar in nature to the pile-up effect, except that it acts in the opposite sense.

Figure 3.20 illustrates the undershoot effect, and shows how it may be compensated for by pole-zero cancellation. A variable resistor is placed in parallel with the capacitor,

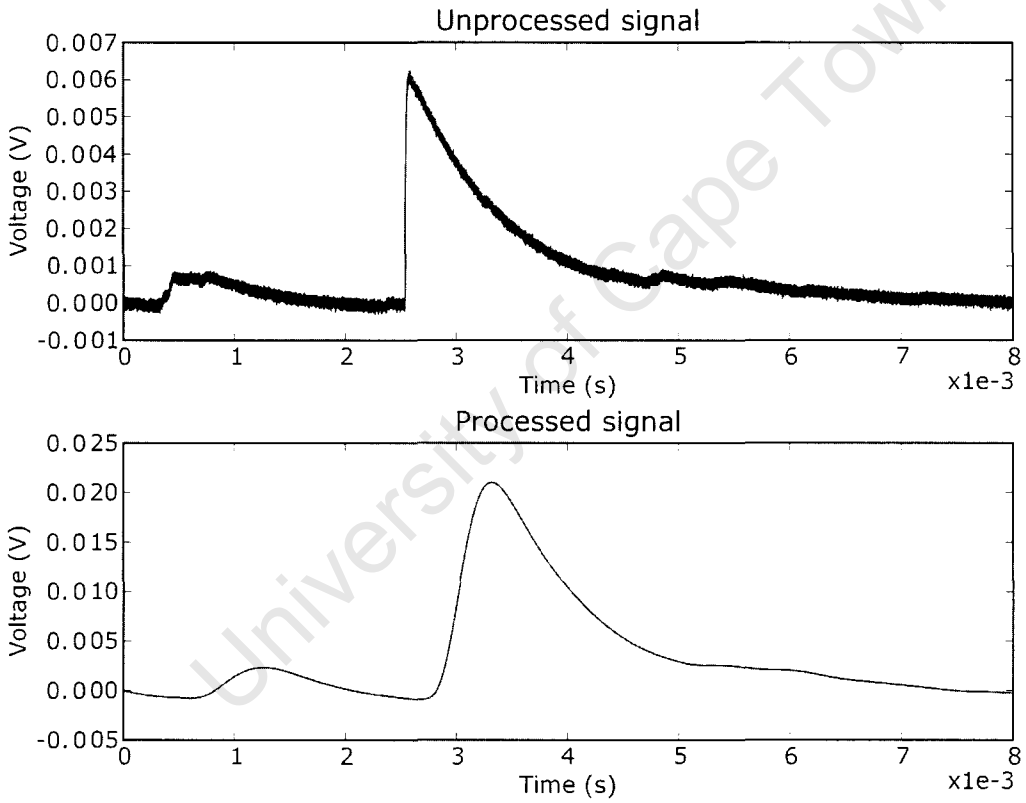

Figure 3.19: The effect of pulse shaping is that, in addition to having the noise filtered out, the tail pulse is transformed into a smooth curve.

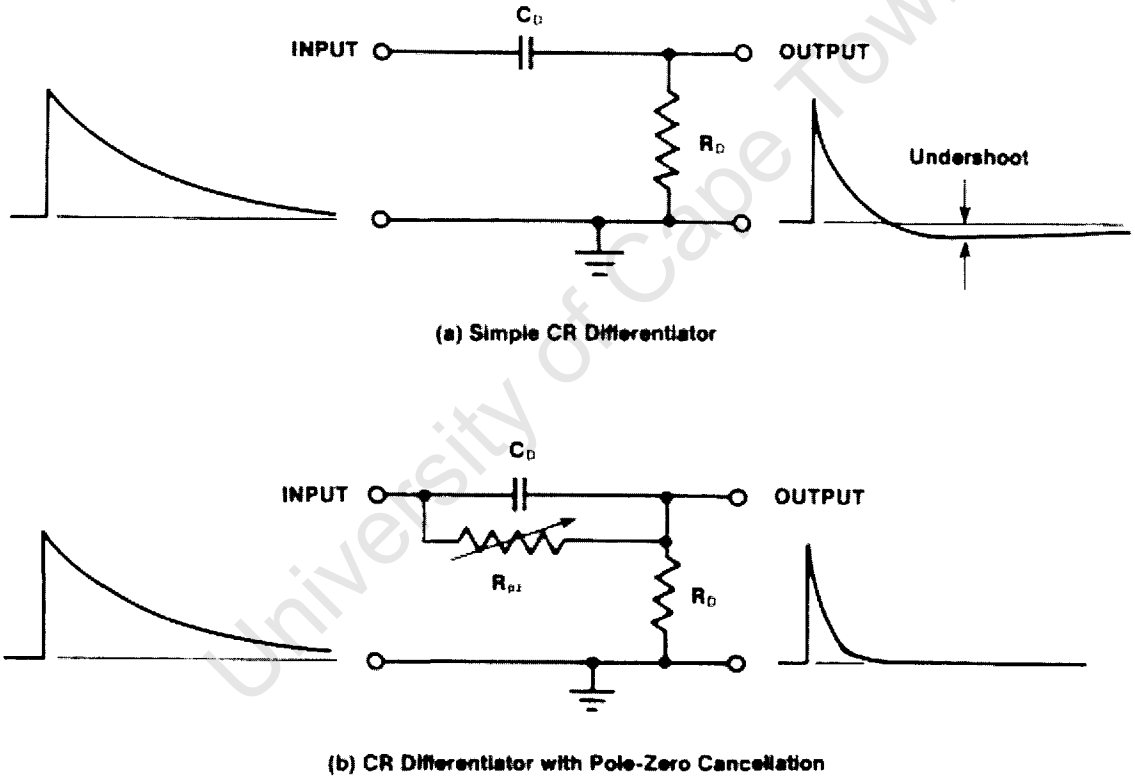

Figure 3.20: The effect of pole-zero cancellation [13].

and the value of the resistance determines the level of compensation. On spectroscopy amplifiers, this is usually adjustable through the front panel. Pole-zero cancellation has been simulated in the digital filter (see Appendix B). The form of the pole-zero term has been inferred from the Ortec amplifier documentation.

3.4 Analysis

In order to determine whether the detector system operates as expected, the experimentally obtained results must be compared with the expected results. The pulse shown in Figure 3.12a will be considered for this purpose. The height of the pulse is difficult to measure with great precision, due to the background signal, but it could be estimated to be between 6.5 mV and 7.0 mV.

The expected voltage is related to the expected deposition of energy in the diode by the proton. To calculate the amount of energy lost by the proton, it is necessary to consider its path from the beam to the diode. The proton must pass through the beam pipe, which is 1.4 mm thick and made of stainless steel [12]. It must then penetrate the 500 μm layer of plastic which coats the photosensitive area of diode, followed by the silicon itself, which has a thickness of 300 μm [15].

The energy loss in each layer was calculated using SRIM[2], a program which uses monte carlo methods to simulate the motion of ions in matter [19]. A summary of the results is shown in Table 3.1. The proton energy shown in the table is the energy of

Table 3.1: Energy loss calculations performed using SRIM.

Proton Energy (MeV)	Material	Thickness (mm)	$\frac{dE}{dx}$ (MeV/mm)	Energy loss (MeV)
200.00	Stainless steel	1.4	2.5	3.5
196.50	Plastic	0.5	0.52	0.26
196.24	Si	0.3	0.86	0.26

the proton *before* entering the relevant material. $\frac{dE}{dx}$ is the energy loss by the proton

[2]The Stopping and Range of Ions in Matter. Available at `http://www.srim.org/`.

per unit length of material. This is essentially the stopping power of the material, with respect to particle energy. The energy loss is the product of $\frac{\mathrm{d}E}{\mathrm{d}x}$ and the thickness of the material. While $\frac{\mathrm{d}E}{\mathrm{d}x}$ is a function of the energy, E, and will therefore vary as the proton travels through the material, it has been assumed to be constant in each layer. This assumption is reasonable, since the energy losses are so small, relative to proton energy, that the increase in $\frac{\mathrm{d}E}{\mathrm{d}x}$ with decreasing E is negligible. The expected energy loss in the silicon was calculated to be 0.26 MeV.

The deposition of energy within the sensitive volume of the silicon results in the creation of electron-hole pairs, as described in §2.3. The amount of energy required to create an electron-hole pair depends on the electronic structure of the material. In silicon, the energy requirement is 3.6 eV/pair. The resultant holes are swept to ground, while the electrons are transported to the charge-sensitive preamplifier, which converts the charge to a voltage signal. In this particular experiment, the preamplifier was an Ortec model 142B, which had a silicon-equivalent[3] charge sensitivity of 20 mV/MeV. Now, the expected voltage, V_{ex}, is given by the product of the energy deposited in the silicon and the silicon-equivalent charge sensitivity of the preamplifier:

$$\begin{aligned} V_{ex} &= 0.26 \text{ MeV} \times 20 \text{ mV/MeV} \\ &= 5.2 \text{ mV}. \end{aligned} \tag{3.26}$$

The observed voltage (as estimated from the Figure 3.12a) is approximately 30% higher than the expected voltage. It should be noted that the calculation of the expected voltage assumed that the proton travelled 300 μm through the silicon, which is the minimum distance possible, and achievable only with a perpendicular path. Most protons would travel through the silicon at some other angle, thereby taking longer paths. Since the energy loss $\Delta E \sim d$, where d is the path length through the material, it is not improbable that a particular proton might have deposited 30% more energy, and thus given rise to 30% more voltage, than the minimum. With such a significant available variation in path lengths and, by extension, voltages, a result of 30% cannot be used to discount the proper operation of the detector. Indeed, it may well support that fact that the device is functioning correctly.

[3]The charge sensitivity is expressed as energy sensitivity using the energy deposited per unit charge liberated in silicon, (3.6 eV) / (1.6×10^{-19} C).

Chapter 4

Implications for future beam loss monitors

4.1 Preamplifier

The project preamplifier has been shown to operate satisfactorily, to the extent that the exponential tail pulses it produced were similar to those produced by the Ortec preamplifiers (see Figure 3.12). The noise characteristics of the custom unit were adequate, though inferior to those of the Ortec models.

The custom preamplifier was found to be vulnerable to electronic pickup, as demonstrated by the 1 kHz component of the signal shown in Figure 3.12b. The preamplifier casing should have functioned as a Faraday cage, thereby shielding the components from stray electromagnetic fields. This effect warrants investigation. The power lines were plain copper with plastic insulation, and these should be shielded to mitigate pickup.

4.2 System packaging

It is recommended that a future detector system be packaged as a single unit, including the detector and the preamplifier. The increased convenience and system portability would be the most apparent benefit of such a development, but the noise characteristics

would also be improved by the decreased capacitance at the preamplifier input, which would result from the elimination of cabling.

The casing material should be chosen to have certain properties. It should be an electrical insulator. This is desirable because it is unacceptable for foreign conducting objects to be brought into contact with any conducting apparatus in the spectrometer vault during an experiment. An insulating case would simplify the procedure of attaching the detector to the beam line pipe.

The material should not have too great a stopping power with respect to the beam particles. For example, acrylic glass has a stopping power of $\frac{dE}{dx} = 0.51$ MeV/mm[1] for 200 MeV protons, which would be acceptable.

The case should provide adequate shielding from stray electromagnetic fields. For compatibility with the requirement that it also be an insulator, it is recommended that there be an inner, conducting layer to provide shielding.

4.3 Proposal of a beam loss monitor array

It has been an objective of this project to design a detector system which could be produced sufficiently cheaply as to allow a large number of units to be distributed around the beam line. A possible scheme for the distribution of the monitors is proposed here.

The proposed monitor array is illustrated in Figure 4.1. Monitors 1-8 are arranged at regularly spaced angular positions, close to the beam line. Monitors 9-12 are arranged at a larger distance from the beam line, such that the monitor pairs (1,9), (3,10), (5,11) and (7,12) are each at equal angular positions.

4.3.1 Beam centring

Monitors 1-8 are used to determine how well the beam is centred. For example, if monitors 8, 1 and 2 were to show significantly higher count rates than monitors 4, 5 and

[1]Calculated using SRIM.

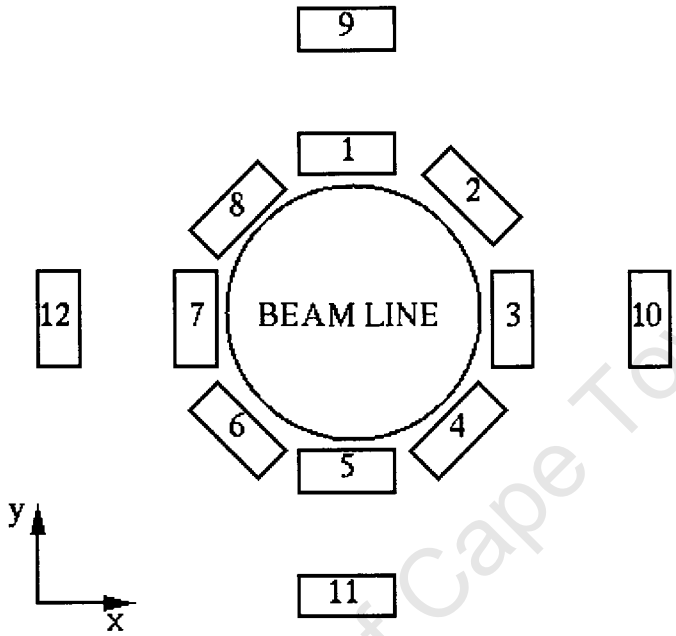

Figure 4.1: Proposed monitor array contains eight monitors at a small distance from the centre of the beam line, at regularly spaced angular positions, as well as four monitors at larger distance from the centre.

6, then that would be an indication that the beam axis is higher than the axis of the beam line pipe.

4.3.2 Beam profile

The beam profile, P, can be treated as a two dimensional Gaussian distribution, given by

$$P = \frac{1}{2\pi\sigma_x\sigma_y} e^{-\left((x-a)^2/2\sigma_x^2+(y-b)^2/2\sigma_y^2\right)}. \tag{4.1}$$

where the centre of the profile is at $(x, y) = (a, b)$ and σ_{xy} is the standard deviation. By treating the x- and y-projections separately, the beam profile can be approximately determined. For example, the x-projection can be found by considering the count rates of monitors 12, 7, 3 and 10. If the count rate is interpreted as a measure of the beam intensity, then fitting the four rates to a Gaussian peak will determine the profile in

the x-projection. An identical procedure using monitors 11, 5, 1 and 9 yields the y-projection.

The number of monitors used in this array was chosen fairly arbitrarily — more or fewer could be used in a real implementation. In particular, more detectors could be used at the outer radius, which would yield a more accurate model of the beam profile.

Chapter 5

Conclusions

The aim of this work has been to develop a cost-effective beam loss monitor for use at iThemba LABS. It is intended that the final product will aid in beam focusing processes, which are, at present, very time-consuming.

A simple and inexpensive charge-sensitive preamplifier, originally designed by R.W. Fearick, has been modified to suit this application. Its performance has been compared with that of a commercially available model, manufactured by Ortec. The simple preamplifier was found to function adequately, despite having inferior noise characteristics and being more prone to electronic pickup of stray signals.

Two beam loss monitor designs were tested. The first was a scintillator-photodiode combination, which used a sample of NE102 plastic scintillator and a Siemens BPW34 p-i-n photodiode. In this design, ionising particles excite molecules in the plastic, prompting fluorescence. The flash of scintillation light enters the sensitive volume of the photodiode, where electron-hole pairs are created. The second design was a photodiode detector, which also used the Siemens BPW34. In this design, ionising particles enter the photodiode directly, prompting electron-hole pair creation. At this stage the charge is swept out to the charge-sensitive preamplifier, which converts it to a voltage signal for further processing.

Signal processing has been carried out on the preamplifier output signals. The methods used were derived from and analysis of RC circuits. Two types of processing were used. The first was noise filtering, by which the high frequency components, which char-

acterise noise, were attenuated. The second type was pulse shaping, which transforms the exponential tail pulses into smoothly varying, bell-like pulses.

Experimentally obtained pulses were analysed and it was found that the voltages were of the same order of magnitude as the theoretical expectations. The wide range of path lengths through the detector, and the corresponding wide range of possible energy losses, are sufficient to account for the discrepancy between the expected voltage and the observed voltage. From this it can be concluded that the beam loss monitor system functions within normal operational parameters.

Recommendations, regarding future improvement of the beam loss monitor, have been made. These focused on reducing the susceptibility of the preamplifier to stray signals, as well as packaging the detector and the preamplifier in one unit. A beam loss monitor placement scheme has been proposed.

Appendix A

Data tables

Table A.1: Photocathode characteristics [11].

Cathode type	Composition	λ at peak response [nm]	Quantum efficiency at peak (%)
S1 (C)	Ag-O-Cs	800	0.36
S4	SbCs	400	16
S11 (A)	SbCs	440	17
Super A	SbCs	440	22
S13 (U)	SbCs	440	17
S20 (T)	SbNa-KCs	420	20
S20R	SbNa-KCs	550	8
TU	SbNa-KCs	420	20
Bialkali	SbRb-Cs	420	26
Bialkali D	Sb-K-Cs	400	26
Bialkali DU	Sb-K-Cs	400	26
SB	Cs-Te	235	10

Table A.2: Physical properties of silicon and germanium [11].

	Si	Ge
Atomic number Z	14	32
Atomic weight A	28.1	72.6
Density [g/cm^2]	2.33	5.32
Dielectric constant (relative)	12	16
Intrinsic resistivity (300 K) [Ωcm]	230000	45
Energy gap (300 K) [eV]	1.1	0.7
Energy gap (0 K) [eV]	1.21	0.785
Electron mobility (300 K) [cm^2/Vs]	1350	3900
Hole mobility (300 K) [cm^2/Vs	480	1900

Appendix B

Source code: digital filter

The following program, written in Python, was used to simulate the action of low-pass and high-pass filters on the data obtained during the beam loss monitor design tests at iThemba LABS. The program has been modified from the original version, written by R.W. Fearick.

```
from pylab import *

"""
Digital signal processing in nuclear physics

classes for amplifier chain

rwf    26 Oct 2006
20 March 2007: more documentation

sdw September 2007

Modified filter process order and file io
"""
class Transfer(object):
    """
    Base class for transfer functions
    """
```

```
19      def __init__(self):
20          self.outm1=0.0
21          self.inm1=0.0
22
23  class LowPass(Transfer):
24      """
25      Low pass filter:
26      l=LowPass(alpha)
27      input: alpha: filter constant
28
29      let dt:      time interval between samples
30          RC:      RC time constant
31      then         alpha=dt/(RC+dt)
32      """
33      def __init__(self, alpha):
34          Transfer.__init__(self)
35          self.a0=alpha
36          self.b1=1-alpha
37      def process(self, insignal):
38          out=self.b1*self.outm1+self.a0*insignal  # LP
39          self.inm1=insignal
40          self.outm1=out
41          return out
42
43  class HighPass(Transfer):
44      """
45      High pass filter:
46      h=HighPass(alpha)
47      input: alpha: filter constant
48      """
49      def __init__(self, alpha, pz=0.0):
50          Transfer.__init__(self)
51          X=1.0-alpha
52          self.a0=((1.0+X)/2)*(1.0+pz)
```

```
53          self.a1=-self.a0*(1.0-pz)
54          self.b1=X
55      def process(self, insignal):
56          """
57          Includes PZ compensation
58          """
59          out=self.b1*self.outm1+self.a0*insignal+self.a1*self.inm1 #HP
60          self.inm1=insignal
61          self.outm1=out
62          return out
63
64  class PreAmp(Transfer):
65      """
66      Preamp simulator: preamp out from delta input
67      h=PreAmp(alpha)
68      input: alpha: filter constant
69      """
70      def __init__(self, alpha):
71          Transfer.__init__(self)
72          self.b1=alpha
73      def process(self, insignal):
74          out=insignal+self.outm1*self.b1
75          self.inm1=insignal
76          self.outm1=out
77          return out
78
79  N=10000
80  t=zeros(N,Float)
81  noise=randn(len(t))
82  output=zeros(N,Float)
83  input=zeros(N,Float)
84  pulse=zeros(N,Float)
85  signal=zeros(N,Float)
86
```

```
87  dt = 1.0                # time between samples (in microseconds)
88  RC = 1.0                # RC time constant (in microseconds)
89
90  pz=0.999*dt/(1+dt)
91  tail=exp(-dt/45.0)
92  alpha=dt/(RC+dt)
93
94  # process chain
95  p1=PreAmp(tail)
96  l1=LowPass(alpha)
97  h1=HighPass(alpha,pz=pz)
98  l2=LowPass(alpha)
99  l3=LowPass(alpha)
100 l4=LowPass(alpha)
101 l5=LowPass(alpha)
102 l6=LowPass(alpha)
103 l7=LowPass(alpha)
104 l8=LowPass(alpha)
105 l9=LowPass(alpha)
106 l10=LowPass(alpha)
107
108 fin=open('some_infile',"r").readlines()
109 fout=open('some_outfile',"w")
110 i=0
111
112 for ll in fin:
113     l=ll.split()
114     t[i]=float(l[0])
115     input[i]=float(l[1])
116     o=l1.process(input[i])
117     o=h1.process(o)
118     o=l2.process(o)
119     o=l3.process(o)
120     o=l4.process(o)
```

```
121         o=l5.process(o)
122         o=l6.process(o)
123         o=l7.process(o)
124         o=l8.process(o)
125         o=l9.process(o)
126         o=l10.process(o)
127         output[i]=o
128         i+=1
129
130 # plot input and output
131 subplot(211)
132 plot(t,input,'b-')
133 title('Unprocessed signal')
134 xlabel('Time (s)')
135 ylabel('Voltage (V)')
136
137 subplot(212)
138 plot(t,output,'b-')
139 title('Processed signal')
140 xlabel('Time (s)')
141 ylabel('Voltage (V)')
142
143 show()
```

Bibliography

[1] J.E Bateman. A solid state scintillation detector for high-energy charged particles. *Nucl. Instr. and Meth.*, 71:261–268, Feb 1969.

[2] P.A.M. Dirac. *The Principles of Quantum Mechanics.* Oxford University Press, fourth edition, 1958.

[3] J.-C. Dousse and Ch. Rhême. The Si photodiode: An inexpensive though high-performing α detector. *Am. J. Phys.*, 51(5):452–455, May 1983.

[4] A. Einstein. Über einen die Erzeugung und Verwandlung des Lichtes betreffenden heuristischen Gesichtspunkt. *Ann. Physik.*, 17:132–148, 1905.

[5] William C. Elmore and Matthew Sands. *Electronics: Experimental Techniques.* National Nuclear Energy Series. McGRAW-HILL BOOK COMPANY, INC, first edition, 1949.

[6] Hamamatsu. *Photomultiplier Tubes: Basics and Applications.* third edition, 2006.

[7] S. Jones. Private communication, 2008.

[8] G. Keil. Gamma-ray spectroscopy with a scintillator-photodiode combination. *Nucl. Instr. and Meth.*, 66:167–172, Sep 1968.

[9] C. Kittel. *Introduction to solid state physics.* John Wiley & Sons, Inc., eighth edition, 2005.

[10] G. F. Knoll. *Radiation Detection and Measurement.* John Wiley & Sons, Inc., 1979.

[11] W.R. Leo. *Techniques for Nuclear and Particle Physics Experiments.* Springer-Verlag, second edition, 1994.

[12] R. Neveling. Private communication, 2008.

[13] Ortec. `http://www.ortec-online.com/electronics/amp/03_4.htm`.

[14] Artem Shevchenko. *Fine Structure of the Isoscalar Giant Quadrupole Resonance from High-Resolution Inelastic Proton Scattering Experiments.* PhD thesis, Technischen Universität Darmstadt, 2005.

[15] Siemens. *Silicon PIN Photodiode.* `http://www.datasheetcatalog.com`.

[16] S. W. Smith. *Digital Signal Processing: A Practical Guide for Engineers and Scientists.* California Technical Publishing, 1997. `http://www.dspguide.com`.

[17] F.D. Smit *et al.* Development of a high energy-resolution zero-degree facility at the iTL K600 magnetic spectrometer. In *Collective motion in nuclei under extreme conditions*, 2006.

[18] H. Fujita *et al.* Better-resolution measurement of vertical scattering angle in a new ion-optical mode of spectrometer "Grand Raiden". *Nuclear Instruments and Methods in Physics Research Section A*, 469(1):55–62, 2001.

[19] J. F. Ziegler *et al. SRIM - the Stopping and Range of Ions in Matter.* Ion Implantation Technology, Incorporated, 2008.

[20] J.L. Conradie *et al.* Cyclotrons at iThemba LABS. In *Cyclotrons and their applications*, 2004.

[21] R. Neveling *et al. Guide to the K600 Magnetic Spectrometer.* iThemba LABS.

[22] Eric W. Weisstein. Z-transform. From MathWorld – A Wolfram Web Resource. `http://mathworld.wolfram.com/Z-Transform.html`.

[23] J.R. Woodyard. Nonlinear Circuit Devices Utilizing Germanium, 1950. US Patent no. 2.530.110.

List of Figures

List of Tables